Research Square

Preprints are preliminary reports that have not undergone peer review.
They should not be considered conclusive, used to inform clinical practice,
or referenced by the media as validated information.

Numerical study on the nonlinear characteristics of shock induced two-dimensional panel flutter in inviscid flow

Hao Zhou
Northwestern Polytechnic University
Gang Wang (wanggang@nwpu.edu.cn)
Northwestern Polytechnical University https://orcid.org/0000-0002-7669-4761
QuanZheng Li
Northwestern Polytechnic University
Yi Liu
Chinese Academy of Sciences

Research Article

Keywords: Shock wave, Panel flutter, Subcritical Bifurcation, Supercritical Bifurcation, Fluid-structure interaction, Limit cycle oscillation

Posted Date: September 30th, 2022

DOI: https://doi.org/10.21203/rs.3.rs-2052840/v1

License: This work is licensed under a Creative Commons Attribution 4.0 International License.
Read Full License

Numerical study on the nonlinear characteristics of shock induced two-dimensional panel flutter in inviscid flow

Hao Zhou[1,a], Gang Wang[2,a,*], QuanZheng Li[3,a] Yi Liu[4,b]

[a] *School of Aeronautics, Northwestern Polytechnical University, Xi'an 710072, P.R. China*

[b] *Institute of Mechanics, Chinese Academy of Sciences, Beijing, 100190, China*

Abstract

For an aeroelastic system of a two-dimensional elastic panel subjected to an impinging inviscid oblique shockwave, the nonlinear flutter characteristics are affected by many factors such as shock impingement location, cavity pressure and initial perturbation. The effects of the above factors on the variation of system bifurcation type and dynamic behaviors are investigated numerically. A low-fidelity computational method coupled with local piston theory and van Karman plate model, and a high-fidelity computational method coupled with Euler equations and finite element model are used for fluid-structure interaction simulations. Two sets of new findings are unveiled. First, either the variation of shock impingement location or cavity pressure can induce the aeroelastic system to transition between a subcritical bifurcation and a supercritical bifurcation. For some cases, the system bifurcation characteristics exhibit strong sensitivity to these two factors. Second, it is found that in addition to the limit cycle oscillation (LCO) in the form of a combination of the second and third structural modes, multiple stable LCOs due to the coupling of

[*] *Corresponding author.*

[1] *PHD Student, School of Aeronautics, National Key Laboratory of Aerodynamic Design and Research; zh2020@mail.nwpu.edu.cn*

[2] *Professor, School of Aeronautics, National Key Laboratory of Aerodynamic Design and Research; wanggang@nwpu.edu.cn*

[3] *PHD Student, School of Aeronautics, National Key Laboratory of Aerodynamic Design and Research; liquanzheng@mail.nwpu.edu.cn*

[4] *PHD; Institute of Mechanics, Chinese Academy of Sciences, liuyi@imech.ac.cn*

higher-order modes can be triggered by proper initial perturbations. These LCOs are attributed with high frequencies and some of them even have high amplitudes, which indicates the higher risk of structural fatigue failure.

Key Words: Shock wave; Panel flutter; Subcritical Bifurcation; Supercritical Bifurcation; Fluid-structure interaction; Limit cycle oscillation

1. Introduction

As the aircraft design moves toward lighter-weight and faster supersonic vehicles, shockwave related aeroelastic problems of thin-wall structures become increasingly import. In recent years, the aeroelastic problem of elastic panels associated with impinging shock waves has attracted a lot of attention from researchers.

Miller et al[1] studied the fluid-thermal-structural interactions on compliant surface panels subjected to shock impingements. The coupling effects as well as the responses to shock motion were investigated. Results showed large initial responses to the imposed loads and shock motion, followed by an obvious reduction of oscillation as the bulking amplitude of the panel became significant. Beberniss et al. [2], and Spottswood et al. [3] carried out several experiments to study the thin panel subject to an impingement oblique shockwave and found clear evidence of fluid-structure coupling that the dynamic response of the structure was greatly increased in the presence of the shock impingement. Willems et al. [4], Pasquariello et al. [5] and Daub et al. [6] also performed similar experiment studies, additionally configuring a fast-moving shock with different ramp angles [7]. Pasquariello et al [5] also carried out a large eddy simulation based fluid-structure coupling analysis of the corresponding experiment. Later, Gogulapati et al. [8] conducted a series computational studies based on the experiments of Beberniss et al. [2] and Spottswood et al. [3] using CFD surrogates combined with Local Piston theory and both full and reduced order structural models. These studies identified several sensitive factors that affect the aeroelastic system, such as thermal state and shock

unsteadiness.

While earlier studies had shown clear coupling features between the shock waves and compliant surfaces, Visbal [9,10], for the first time, elucidated the flutter characteristics of an elastic panel subject to an impinging oblique shock wave by performing high-fidelity computational fluid dynamics/computational structural dynamics coupling simulations in both inviscid and laminar flow regimes. The results showed that the aeroelastic system with shock impingement behaves completely different from that of the traditional panel flutter. Depending on the shock strength, either supercritical or subcritical bifurcations emerged at a value of dynamic pressure which could be considerably lower than that corresponding to classic panel flutter [9]. In addition, the laminar cases [10] showed the coupling of boundary layer instabilities with higher-order structure modes, and complex non-periodic self-excited oscillations of multiple higher frequencies were observed. Shahriar et al. [11] also studied the shock wave laminar boundary layer interaction over a compliant surface, and effects of different thermal boundary conditions were investigated. Building on Visbal's work [9], Boyer et al. [12] examined the features of shock-induced panel flutter in three-dimensional inviscid flow and found very similar dynamic characteristics near the centerline. However, away from the centerline, the three-dimensional effects showed significant influence on the solution. Shinde et al. [13] continued the work of [9,10,12] and further studied the transitional shock boundary layer interaction over a flexible panel by performing direct numerical simulations. It was found that the presence of flexible panel can promote flow transition. They also investigated the effect of several structural parameters on the shock wave boundary layer induced panel flutter [14]. In addition to these studies, recently, more experiments and numerical studies focus on the fluid-structure coupling of flexible panels with shock turbulent boundary layer interactions [15-22]. Among them, Daub et al. [20] observed panel flutter phenomena in the experimental study of fluid-structure interactions between elastic panel and incident shock wave boundary layer interaction. It was

identified that the dynamics of the panel were strongly influenced by the thermal state of structure, and the structure failure due to flutter were found in the experiment. Shinde et al. [21] investigated the shock wave turbulent boundary layer interaction over a flexible panel by performing large eddy simulations (LES) with fluid-structure coupling method, and modal analysis were carried out to identify the coupling between system components. Zope et al. [22] studied dynamics of the oblique shock wave and turbulent boundary layer with a flexible panel by using hybrid Reynolds averaged Navier-Stokes/large eddy simulation (RANS/LES) methods and compared the predictive capabilities of low-fidelity and high-fidelity turbulence modelling approaches.

Although experimental studies are the most direct way to explore the fluid-structure coupling phenomena of the shock dominated aeroelastic problems, the research can be impeded by experimental facilities and measurement methods. In contrast, the high-fidelity multi-physics simulations are not limited by these limitations, and complete physical field data can be obtained much easier. However, the high-fidelity turbulent modelling method such as LES and DNS are computationally expensive and not suitable for long-time fluid-structure coupling simulations. Moreover, even using RANS-based or Euler-based fluid-structure coupling methods may also be unaffordable for detailed parameter studies on three-dimensional problems. It is probably for these reasons that most of the published literatures only address a few system states and lack detailed system studies. Driven by the needs for fast prediction of long-time nonlinear responses, there are ongoing researches on the system modelling methods and their applications [8,23-29]. Brouwer et al. [24] proposed an enriched piston theory for aerodynamic loads prediction in the presence of shock impingements, and it was then extended to incorporate flow nonlinearities by combining a nonlinear autoregressive with exogenous inputs model [25]. Ye et al. [27,28] conducted theoretical analyses of the aeroelastic stability of heated elastic and viscoelastic panels in shock dominated

inviscid flows based on the local piston theory. The Subsequent study [29] identified the importance of interplay between the static pressure differential and the unsteady dynamic pressure.

Despite the influence of boundary layer in practical scenarios, the inviscid cases can still provide a good theoretical reference for related studies. In the studies mentioned above, the subcritical bifurcation characteristics of the shock induced panel flutter were observed in both the inviscid and viscous flow [9,10,25]. As the subcritical bifurcation tends to be more dangerous than supercritical bifurcation in engineering [30-33], understanding the system bifurcation behavior is of great importance in the aircraft structural design. Visbal [9] noted that increasing the shock strength can drive the system transition from a subcritical bifurcation to a supercritical bifurcation. In general, the bifurcation type of an aeroelastic system does not depend solely on one factor. Identifying all factors that affect the bifurcation characteristics of the system will be helpful for future bifurcation control. However, to date, there are very few published literatures have considered whether other factors can affect the bifurcation type of the current aeroelastic system.

The current study serves as a complementary work of the shock-dominated aeroelastic problems in inviscid flow regime. The effects of several factors on the variation of system nonlinear bifurcation characteristics are addressed, including the shock impingement location, cavity pressure and initial perturbation. Although one or more of these factors were discussed in some of the reviewed studies, none of them have clarified that how the system bifurcation characteristics, especially the bifurcation type, are affected by these factors due to the limited parameter states studied. In this paper, the variation trends of the system bifurcation type as well as the changes of system dynamic behaviors with these factors are unveiled through detailed numerical simulations. A low-fidelity and a high-fidelity computational framework are established for the fluid-structure coupling analysis. The low-fidelity framework is used for fast prediction and drawing basic conclusions due to its high efficiency, while

the high-fidelity framework is used for performing confirmatory calculations on the obtained conclusions, thereby improving the overall analysis efficiency.

The remainder of this paper is organized as follows. A brief description of physis modelling and introduction of numerical methods are given in section 2. The results and discussions of are detailed in section 3. Concluding remarks are summarized in section 4. Validations of developed computational frameworks are provided in Appendix.

2. Physics modelling

The physical domain of the present work is shown in Fig. 1. An elastic panel with length l and thickness h is placed in an inviscid supersonic fluid domain with an impinging shock and a reflecting shock. β denotes the shock wave angle of the impinging shock and x_i denotes the impingement location. M_∞, U_∞ and ρ_∞ denotes the Mach number, velocity as well as the density of the incoming flow. The fluid domain is divided into three subdomains by the shock waves, whose static pressures are p_1, p_2 and p_3 respectively. p_c denotes the cavity pressure. Noted the current research focuses on the two-dimensional analysis and the conclusions drawn in this study may only be applicable to the panels with high aspect ratio. However, the results in Ref. [34] show that the aeroelastic properties of the centerline of the three-dimensional cases are very close to that of two-dimensional cases. This indicates that the two-dimensional cases are still of practical reference value to the three-dimensional problems, and the effects of aspect ratio are left for future investigations. In this study, a low-fidelity and a high-fidelity computational framework are established for the fluid-structure coupling analysis.

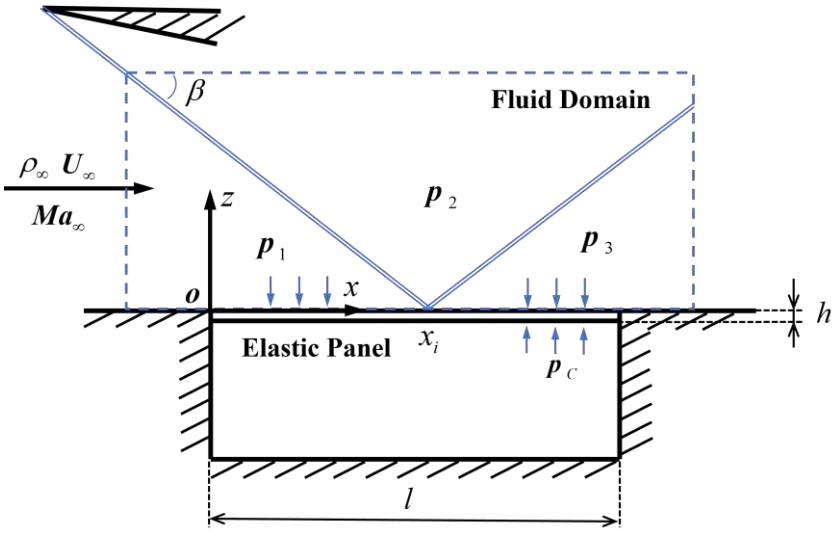

Fig. 1 Panel geometry and flow condition

2.1 Fluid Modeling

For the low-fidelity computational framework, the instantaneous fluid pressure $p(x,y,t)$ acting on the panel upper surface is modeled by local piston theory [35]. Considering the low Mach number flow regime behind the reflecting shock wave, the second order supersonic flow theory of Van Dyke [36] is used to define the piston theory coefficient

$$p(x,y,t) = p_l + \gamma p_l \left[\frac{M_l}{\sqrt{M_l^2 - 1}} \frac{w_n}{a_l} + \frac{M_l^4(\gamma+1) - 4(M_l^2 - 1)}{4(M_l^2 - 1)^2} \left(\frac{w_n}{a_l} \right)^2 \right] \tag{1}$$

where, p_l and a_l denote the local surface pressure and the local sonic speed respectively. M_l denotes the local Mach number. w_n is the piston speed, sometimes referred to as downwash speed. It is defined by

$$w_n = U_l \frac{\partial z}{\partial x} + \frac{\partial z}{\partial t} \tag{2}$$

where U_l denotes the local flow velocity. The local flow flied properties denoted by the subscript l can be extracted from the steady computational fluid dynamics (CFD) simulation results over an undeformed panel surface, which is considered to capture the prominent characteristics of the flow field with shock impingement.

For the high-fidelity computational framework, the fluid pressure is obtained through the CFD method. A well validated in-house CFD solver HUNS3D [4,5] with mesh deformation capabilities is used to solve the flow field. The Arbitrary Lagrangian-Eulerian formulation of the Euler equation is adopted to model the fluid field with boundary movement, and the integral form of the governing equation for a bounded control volume Ω with boundary $\partial\Omega$ is as follows

$$\frac{\partial}{\partial t}\iiint_{\Omega}\boldsymbol{U}d\Omega+\iint_{\partial\Omega}\boldsymbol{F}(\boldsymbol{U},\boldsymbol{V}_{grid})\cdot\boldsymbol{n}dS=0 \tag{3}$$

In Eq. (3), $\boldsymbol{U}=\{\rho,\rho u,\rho v,\rho w,\rho E\}^{\mathrm{T}}$ represents the conservative variables, and $\boldsymbol{F}$ denotes the convective flux. $\boldsymbol{V}_{grid}$ denotes the grid velocity vector. The equation is discretized on unstructured meshes with the cell-centered finite volume method. For each mesh cells Ω_i, Eq. (3) can be written as

$$\frac{d(\Omega_i\boldsymbol{U}_i)}{dt}+\sum_{m\in N(i)}\boldsymbol{F}(\boldsymbol{U}_m,\boldsymbol{V}_{grid,m})\boldsymbol{S}_m=0 \tag{4}$$

where the $N(i)$ denotes the total number of faces of each mesh cell. The flux term is discretized using Roe's [37] method, and the second order accuracy is achieved by the piecewise linear reconstruction method of Barth and Jespersen [38]. The time derivative is discretized using the second order forward difference scheme. Eq. (4) can be then rewritten in the form of

$$\frac{3(\Omega_i\boldsymbol{U}_i^{n+1})-4(\Omega_i\boldsymbol{U}_i^{n})+(\Omega_i\boldsymbol{U}_i^{n-1})}{2\Delta t}+\boldsymbol{R}_i(\boldsymbol{U}_i^{n+1})=\boldsymbol{0} \tag{5}$$

Eq. (5) is integrated in time using an implicit dual-time-stepping approach implemented in the CFD solver, and the Geometric Conservation Law [39] is satisfied during solver implementation.

A stretched structural mesh is constructed for the initially undeformed panel. The mesh is discretized using 351×101 nodes in the streamwise and wall normal direction. 201 points are evenly distributed on the surface of the elastic panel, which is finer than that used in Ref. [9]. The two-dimensional mesh is further extruded by one layer spanwise to generate a 3D mesh that suitable for the CFD solver, and the

symmetry boundary condition is applied in the spanwise direction to enable a two-dimensional solution. The left and right boundaries of the fluid domain in Fig. 1 are prescribed as far field, and the upper boundary is imposed according to the oblique shock relations. The lower boundaries including the elastic panel surface are prescribed as slip wall. The fluid surface mesh of the elastic panel is also used for the local piston theory. As will be demonstrated later, the mesh is fine enough to capture all the phenomena of interest in this study.

2.2 Structure Modeling

In the low-fidelity computational framework, a previously developed structural dynamics solver [40,41] based on the von Kármán large-deflection equation for semi-infinite plates [42] has been used. The governing equation of the structure dynamics is as follows

$$\rho_s h \frac{\partial^2 w}{\partial t^2} + D \frac{\partial^4 w}{\partial x^4} - N_x \frac{\partial^2 w}{\partial x^2} = p_c - p \tag{6}$$

In Eq.(6), the panel's displacement w in z direction is described as a function of coordinate x and time t. ρ_s and h represents the density and thickness of the elastic panel, respectively. $D = Eh^3 \big/ 12\left(1-\nu^2\right)$ is the equivalent bending stiffness of the panel. E is the Young's modulus and ν is the Poisson's ratio. p_c represents net cavity pressure acting on the panel lower surface. N_x is the in-plane additional tension caused by the geometric nonlinearities, and the specific mathematical form of N_x is given in Eq. (7), where l is the length of panel.

$$N_x = \frac{Eh}{2l\left(1-\nu^2\right)} \int_0^l \left(\frac{\partial w}{\partial x} \right)^2 dx \tag{7}$$

Eq.(6) is discretized using Galerkin's method with the expansion of the displacement in the form of

$$w(x,t) \approx h\sum_{i=1}^{N} q_i(t)\sin\left(i\pi\frac{x}{l}\right) \tag{8}$$

where q_i denotes the Galerkin's mode coefficient. The discretized form of Eq.(6) is as follows

$$\begin{aligned}\frac{\rho h l^4}{D}\frac{d^2 q_j(t)}{dt^2} + (j\pi)^4 q_j(t) + 3(j\pi)^2\left[\sum_{k=1}^{N}\left(k\pi q_k(t)\right)^2\right]q_j(t) = \\ -\frac{2l^4}{Dh}\int_0^l (p-p_c)\frac{1}{l}\sin\left(j\pi\frac{x}{l}\right)dx \qquad j = 1,2\text{L}\ ,N\end{aligned} \tag{9}$$

The right term of Eq. (9) represents the generalized aerodynamic force. It is denoted as $f_{a,j}$ in the following text, which is an element of the generalized aerodynamic force vector $\boldsymbol{f}_a$. By introducing a state vector $\boldsymbol{e} = \left[e_1,\text{L}\ ,e_N,e_{N+1},\text{L}\ ,e_{2N}\right]^{\text{T}} = \left[q_1,\text{L}\ ,q_N,\frac{\partial q_1}{\partial t},\text{L}\ ,\frac{\partial q_N}{\partial t}\right]^{\text{T}}$, Eq. (9) can be rewritten as a system of first order ordinary differential equations

$$\begin{cases}\dfrac{de_j}{dt} = e_{N+j} \\ \dfrac{de_{j+N}}{dt} = \dfrac{D}{\rho h l^4}\left\{-\left[(j\pi)^4 - \dfrac{N_0 l^2}{D}(j\pi)^2\right]e_j(t) - 3(j\pi)^2\left[\sum_{k=1}^{N}\left(k\pi e_k(t)\right)^2\right]e_j(t) + f_{a,j}\right\}\end{cases} \qquad j = 1,2,\text{L}\ ,N \tag{10}$$

Eq. (10) is solved by an modified Runge-Kutta scheme implemented in the structural dynamic solver[40]. Dowell [42] states that the system converges with six Galerkin's modes. However, considering the possibility of higher order mode instability, the first twelve order streamwise modes are selected for the simulation in this study.

In the high-fidelity computational framework, the structure is discretized using the finite element method, this can be done by any standard finite element method software packs such as Calculix [43] and Abaqus [44]. In the present work, Abaqus is chosen as the computational structural dynamics (CSD) solver, and the elastic panel is modeled with S4R type shell element, which is used to simulate the finite strains and

large deformations. 100 shell elements are evenly distributed on the streamwise direction, and symmetry boundary conditions are applied to the spanwise direction to enforce a two-dimensional solution. The boundary conditions for the leading and trailing edges are specified as pinned. The final discretized structural dynamic equations can be written in the following form of

$$[\boldsymbol{M}]\ddot{\boldsymbol{u}} + [\boldsymbol{C}]\dot{\boldsymbol{u}} + [\boldsymbol{K}]\boldsymbol{u} = \boldsymbol{F} \tag{11}$$

where $[\boldsymbol{M}]$ denotes the mass matrix, $[\boldsymbol{C}]$ denotes the damping matrix, $[\boldsymbol{K}]$ denotes the stiffness matrix, and $\boldsymbol{F}$ denotes the loads vector. $\boldsymbol{u}$ is the structural deformation vector. Note that $[\boldsymbol{M}]$ and $[\boldsymbol{C}]$ are assumed to be constant, and $[\boldsymbol{C}]$ can be neglected if no structural damping is involved. The stiffness matrix $[\boldsymbol{K}]$ is dependent on displacements due to the geometric nonlinearities. Eq. (11) are solved using an implicit time integration method proposed by Hilber et al. [45]

2.3 Fluid-Structure Coupling

The fluid dynamics solver and structural dynamics solver are coupled using a partitioned approach, and the coupling stability as well as time accuracy are preserved with a combination of a polynomial aerodynamic load estimator. Similar approaches were adopted in Ref. [46,47]. The flow chart of complete fluid-structure coupling procedure is shown in Fig. 2. The left branch of the flow chart represents the high-fidelity framework coupled with finite volume method (FVM) and finite element method (FEM), and the right branch represents the low-fidelity framework coupled with local piston theory (LPT) and Galerkin's method. The high-fidelity and low-fidelity computational frameworks will be referred to as LF and HF respectively in the following text. The details of the fluid-structure coupling procedure is introduced as follows and the validation of the fluid structure coupling scheme and solver implementations are given in the Appendix.

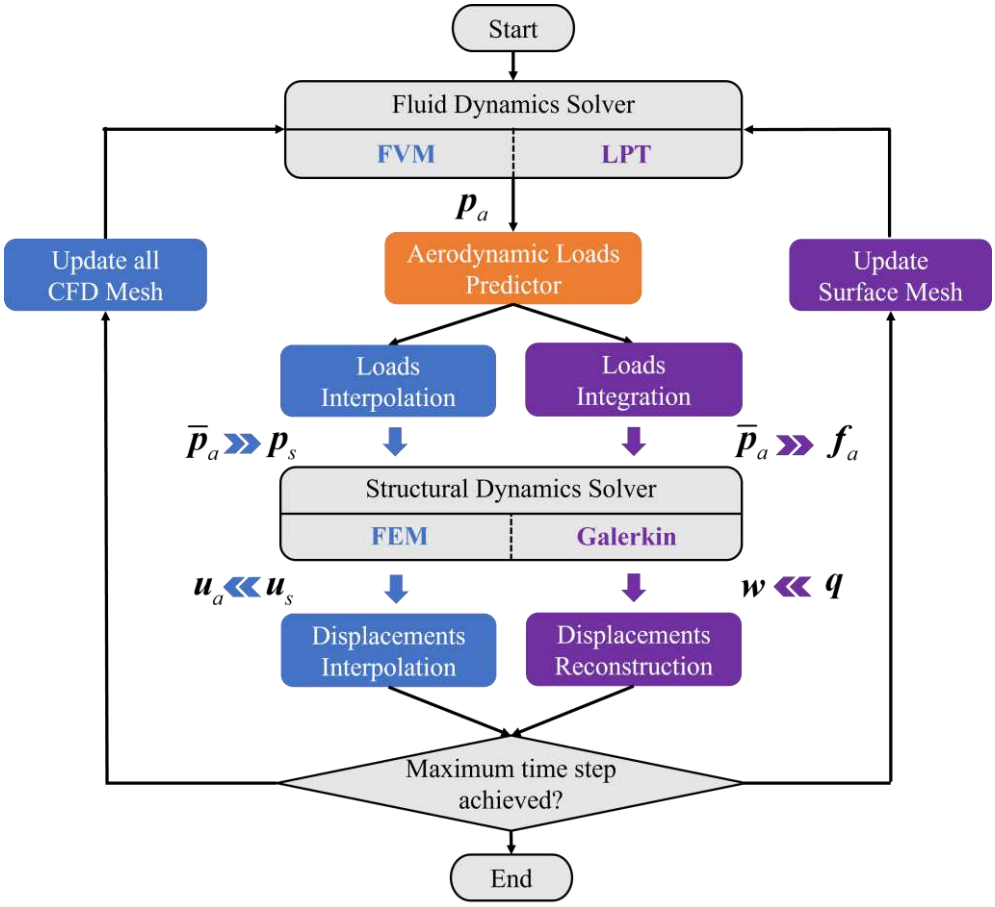

Fig. 2 Fluid-structure coupling procedure

For time step $n+1$, the aerodynamic loads $\boldsymbol{p}_a$ at time step n obtained from the fluid dynamic solver is passed to the aerodynamic loads predictor. The loads predictor predicts $\bar{\boldsymbol{p}}_a$ at time step $n+1$ based on the aerodynamic loads at previous time steps according to the Lagrange's interpolation formula

$$\bar{\boldsymbol{p}}_a^{\,n+1} = \sum_{j=0}^{N} l_j \boldsymbol{p}_a^{\,n-j} \tag{12}$$

in which, l_j is defined as

$$l_j = \frac{\prod_{i=0;i\neq j}^{N} \left(t_{n+1} - t_{n-i}\right)}{\prod_{i=0;i\neq j}^{N} \left(t_{n-j} - t_{n-i}\right)} \tag{13}$$

In this study, the second order interpolation formula (N=2.) is employed. For the constant time step, Eq. (12) can be simplified as

$$\bar{\boldsymbol{p}}_a^{\,n+1} = 3\boldsymbol{p}_a^{\,n} - 3\boldsymbol{p}_a^{\,n-1} + \boldsymbol{p}_a^{\,n-2} \tag{14}$$

$\bar{\boldsymbol{p}}_a$ is then passed to the structural dynamic solvers.

In the high-fidelity computational framework, the surface meshes of the fluid-structure boundary do not match. The RBF interpolation method [48] is used for the information exchange between the structure domain and fluid domain. The predicted aerodynamic loads $\bar{\boldsymbol{p}}_a$ are interpolated from the fluid surface mesh to the structure surface mesh, and the solved structural displacements $\boldsymbol{u}_s$ are interpolated from the structure surface mesh to the fluid surface mesh. The interpolated loads and displacements are denoted as $\boldsymbol{p}_s$ and $\boldsymbol{u}_a$ respectively. When $\boldsymbol{u}_a$ is obtained and the maximum number time steps is not reached, the RBF mesh deformation method is used to update the CFD mesh [49].

In the low-fidelity computational framework, the generalized aerodynamic force vector $\boldsymbol{f}_a$ is obtained by integrating $\bar{\boldsymbol{p}}_a$ over the elastic panel surface through Eq. (15)

$$f_{a,j} = -\frac{2l^4}{Dh}\int_0^l (p - p_c)\frac{1}{l}\sin\left(j\pi\frac{x}{l}\right)dx \qquad j = 1, 2\mathrm{L}\ , N \tag{15}$$

where $f_{a,j}$ is the element of $\boldsymbol{f}_a$. The surface displacement vector $\boldsymbol{w}$ is reconstructed by Eq. (8) once the Galerkin's mode coefficient vector $\boldsymbol{q}$ is solved by the structural dynamics solver. The surface mesh will be updated if the maximum number time steps is not reached.

The dimensional analysis shows that the aeroelastic system are governed by several non-dimensional parameters [27]. The aerodynamic parameters include the Mach number M_∞, the pressure ratio p_3/p_1 and the non-dimensional dynamic pressure $\lambda = \rho_\infty U_\infty^{\,2} l^3/D$. The structural parameters include the mass ratio $\mu = \rho_\infty l/\rho_s h$ and the thickness-length ratio h/l. In this study, the fluid-structure

coupling analysis is carried out at M_∞=2.0, and the elastic panel has the structural parameters of μ=0.1, h/l=0.002, which corresponds to the previous study of Ref. [9]. The non-dimensional dynamic pressure in the range of 100<λ<1000 is mainly considered, and the time step is selected to ensure the convergence of the time domain response.

Among the relevant studies[9,10], the fluid-structure coupling simulations are generally started from a converged steady solution of a rigid panel, or started by changing λ from a previous case. However, these approaches cannot directly control the amplitude of the initial perturbation, which is inconvenient to study the influence of the initial perturbation on the aeroelastic system. In order to fully control the initial perturbation for starting the fluid-structure coupling simulation, different approaches are used in this study. A steady fluid-structure coupling analysis is first carried out to obtain a converged static aeroelastic equilibrium state. Then, an initial velocity field perturbation in the form of $dw/dt\big|_{t=0} = a_0 h \sin\left(i\pi x/l\right)$ is applied to the elastic panel to start the unsteady fluid-structure coupling simulation. a_0 denotes the amplitude of perturbation, and the integer i controls the distribution of the initial velocity field, which corresponds to the i th order of the structural mode. As the steady fluid-structure coupling analysis shows that the panel deflects in an approximate second-mode characteristic, the unsteady fluid-structure coupling simulation is initiated by a second mode velocity perturbation (i=2). The perturbation amplitude a_0 is increased from a small value until the limit cycle oscillation occurs.

3. Results and discussion

3.1 Baseline， Ma=2.0, P3/P1=1.8

The first set of cases are carried out at Mach 2.0 with the shock strength of P3/P1

= 1.8, which is used as an additional validation of present computational frameworks. Sufficiently long time of fluid-structure interaction simulations are carried out to obtain the stable limit cycle oscillations (LCOs) of different non-dimensional dynamic pressure λ. The amplitude and frequency curves at x_i/l=75% are drawn in Fig. 3, together with the results from other literatures. The nondimensional frequency K_f is defined as $K_f = f \cdot l/U_\infty$, where f is the frequency and U_∞ is the incoming flow velocity.

As can be seen in Fig. 3(a), all the amplitudes of limit cycle oscillations agree well each other when λ>600, except for the results predicted by Brouwer and McNamara [24] with enriched piston theory method (EPT), which are obviously lower than other results. In Fig. 3(b), Brouwer and McNamara [24] also predicted higher LCO frequencies than others. Such difference is likely caused in part by the reduced applicability of piston theory to the low Mach number flow behind the reflecting shock wave. Noted that the amplitudes predicted by the current low-fidelity framework are only slightly higher than that predicted by the high-fidelity framework, while the frequencies are slightly lower. The time-space diagram of the elastic panel for λ=600, 800, 1000, are shown in Fig. 4 to provide a more intuitive view of system responses. It is shown that the panel vibrates in the form of an approximate second-mode shape with slightly higher fluctuations near the trailing edge, which is consistent with that described in Ref [9,10]. The coupled modes seem unchanged as λ increases. For λ<600, discrepancies appear among all results. In Fig. 3(a). The results predicted by Visbal [9] and Brouwer and McNamara [24] show that the flutter onset displays the features of a supercritical bifurcation, while the results of XiaoMin An [50] and that predicted by the current high-fidelity framework show the features of a subcritical bifurcation. The low-fidelity framework also predicts the characteristics of a subcritical bifurcation. Besides, the predicted bifurcation point is much higher than that predicted by the high-fidelity framework. It should be mentioned that a large

initial velocity perturbation is required to excite the system into limit cycle oscillations in the subcritical bifurcation state. The discrepancies of bifurcation type can be caused by the differences in numerical methods and code implementations. However, the cases to be discussed later show that the discrepancies may also be due to the sensitivity of the aeroelastic system to the shock impingement condition.

In addition, for the current case, the results predicted by the two frameworks are only quantitatively different. Considering the high efficiency of the low-fidelity framework, in the following cases, it is first used for conducting more detailed parametric studies and drawn basic conclusions. Then, the high-fidelity framework is used to verify the results under typical conditions to ensure the applicability of the conclusions.

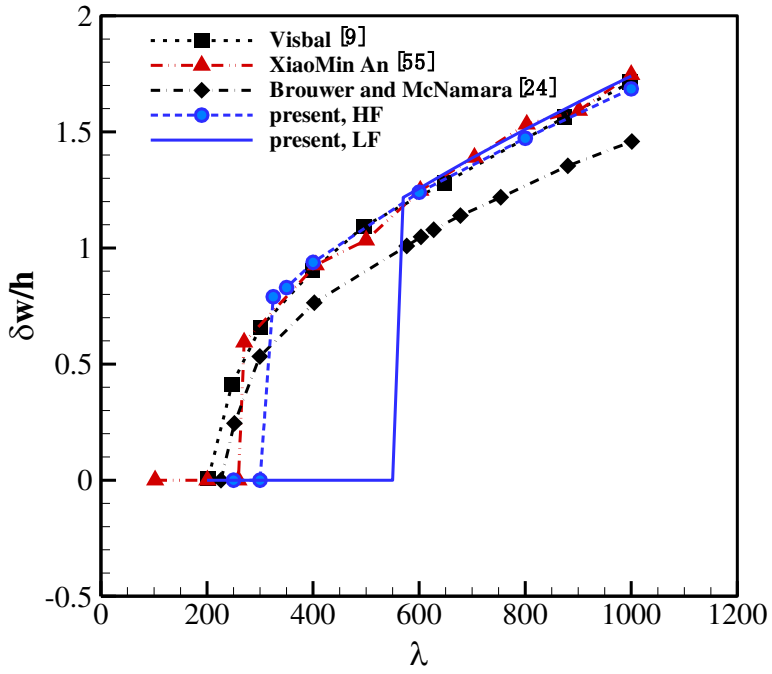

(a) LCO amplitude at 75% chord length

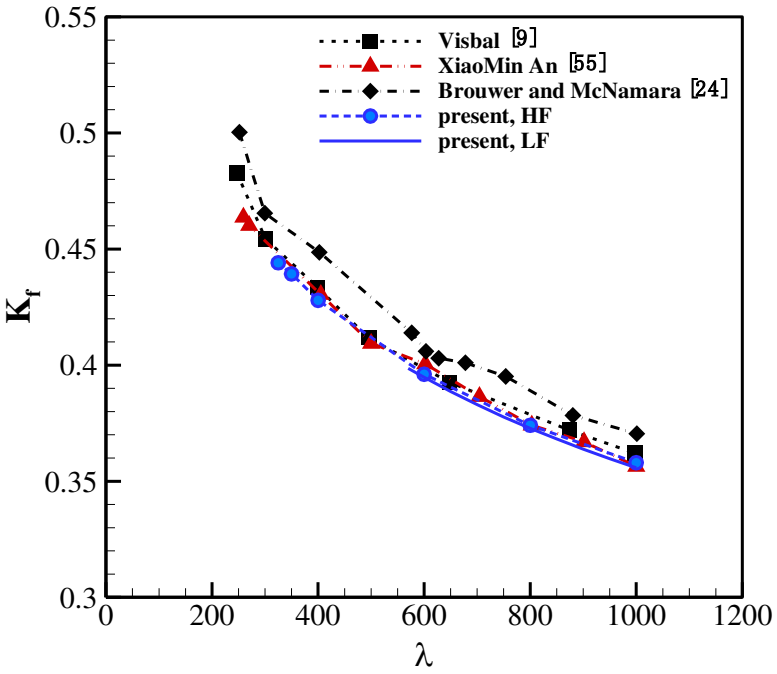

(b) Dominant LCO frequency at 75% chord length

Fig. 3 LCO curves at Ma=2.0, P3/P1=1.8, Ma=2.0

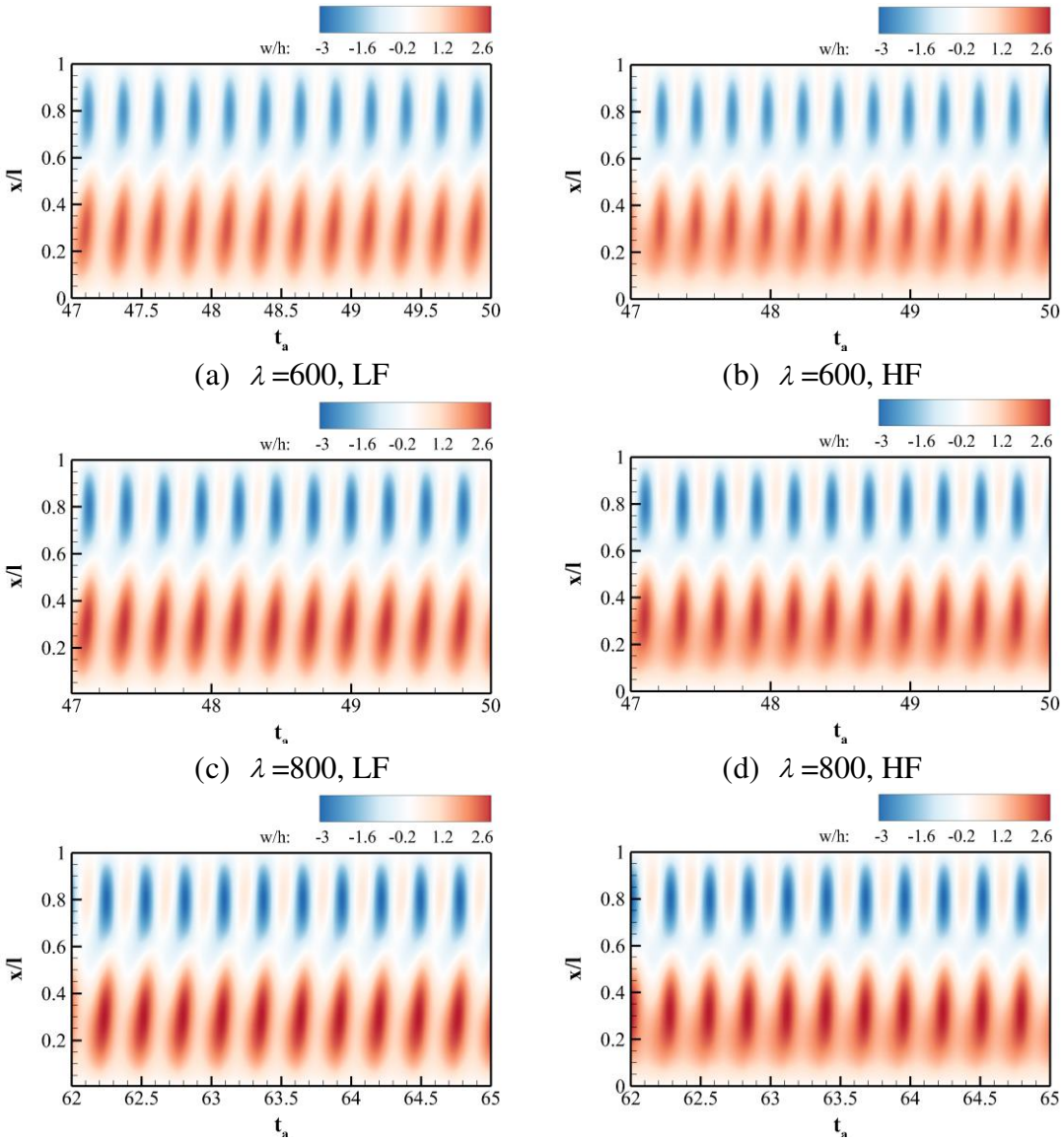

(a) λ=600, LF (b) λ=600, HF

(c) λ=800, LF (d) λ=800, HF

(e) λ=1000, LF (f) λ=1000, HF

Fig. 4 x-t diagram of panel deflection, P3/P1=1.8, P_C=1.4, Ma=2.0

3.2 Effect of the impingement location

In order to investigate the effects of the shock impingement location on the variation of the bifurcation characteristics, a set of fluid-structure interaction simulations are carried out with impingement locations ranging from x_i/l=50% to 42% with cavity pressure being constant. This is slightly different from that of Ref. [9] where the cavity pressure varies as the impingement point moves.

The predicted LCO amplitude curves and frequency curves are shown in Fig. 5(a)

and (b), respectively. In Fig. 5(a), as the impingement point moves to the left, the system bifurcation point also moves to the left. Meanwhile, the system bifurcation type gradually transitions from a subcritical bifurcation to a supercritical bifurcation. When x_i/l is less than 47%, the low-fidelity framework predicts that the bifurcation point starts to move to the right gradually. In addition, for a given value of λ, the LCO amplitude reduces as the impingement point moves forward. In Fig. 5(b), the frequency increases continuously as the shock impingement location moves to the leading edge of the elastic panel. These variation trends of bifurcation characteristics have been well validated by the high-fidelity computational framework.

Noted that when the impingement point is near the center of the elastic panel, the bifurcation characteristics of the aeroelastic system seems to be very sensitive to the shock impingement location. Even a 1% shift in panel length can lead to significant changes in bifurcation point or even changes in bifurcation type. In numerical simulations, the actual shock wave impingement location can be affected by many factors, such as grid resolution, shock wave generation method, and the choice of limiter functions. All these could introduce uncertainties to the shock impingement location, thus leading to possible discrepancies in bifurcation characteristics predicted by different researchers.

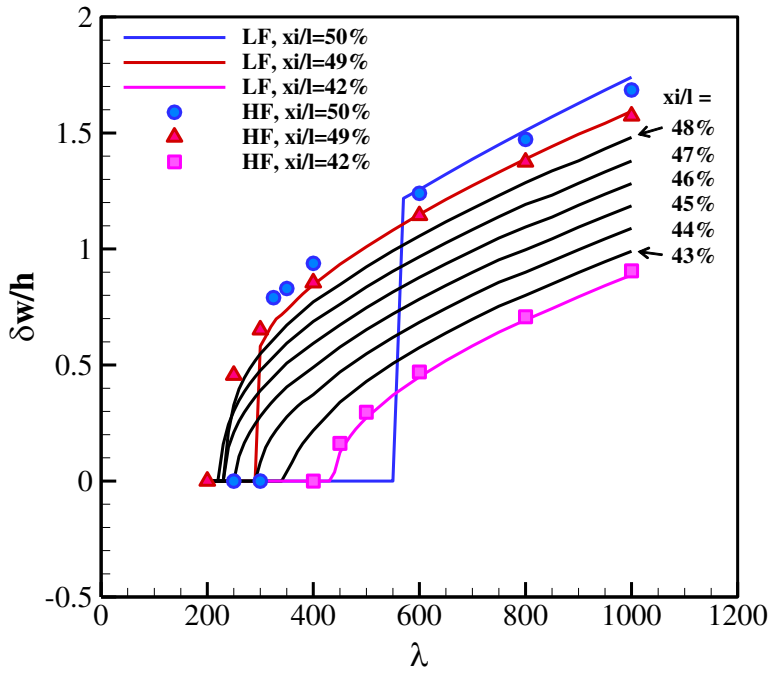

(a) LCO amplitude at 75% chord length

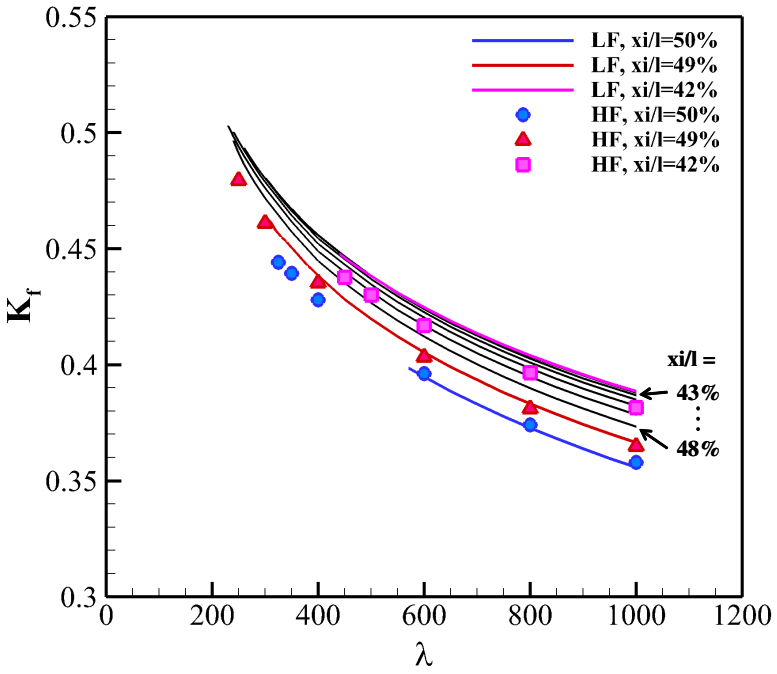

(b) Dominant LCO frequency at 75% chord length

Fig. 5 Effects of the impingement location on the LCOs, P3/P1=1.8, Ma=2.0

In addition to monitoring the responses at a specific point on the elastic panel, the displacement vectors are projected onto the structure's natural modal coordinate system to show the modal participation of the limit-cycle oscillations. Noted that for the current case, the Galerkin's mode is identical to the structural natural mode. Here the mode amplitude is still denoted by q. Fig. 6(a-c) shows the modal participation variation with λ for the shock impingement locations of x_i/l=50%, 49% and 42%, respectively. The mode amplitudes are normalized by the second mode. It can be seen from these figures that the proportion of the second and third modes is much higher than that of other modes, and the modal participation predicted by the two computational frameworks are basically consistent. In Fig. 6(a) and Fig. 6(b), the second mode has the largest proportion, and the proportion of the third mode increases gradually with the increase of λ. It seems that the proportion of the third mode reaches a plateau around λ=800. Comparing the results in Fig. 6(a) and Fig. 6(b), it can be found that for a given λ, the proportion of the third mode also increases as the impingement location moves forward. When the impingement location moves to x_i/l=42%, as shown in Fig. 6(c), the proportion of the third mode has exceeded that of the second mode. In addition, for a fixed shock impingement location, the proportion of the third mode gradually decreases with the increase of λ.

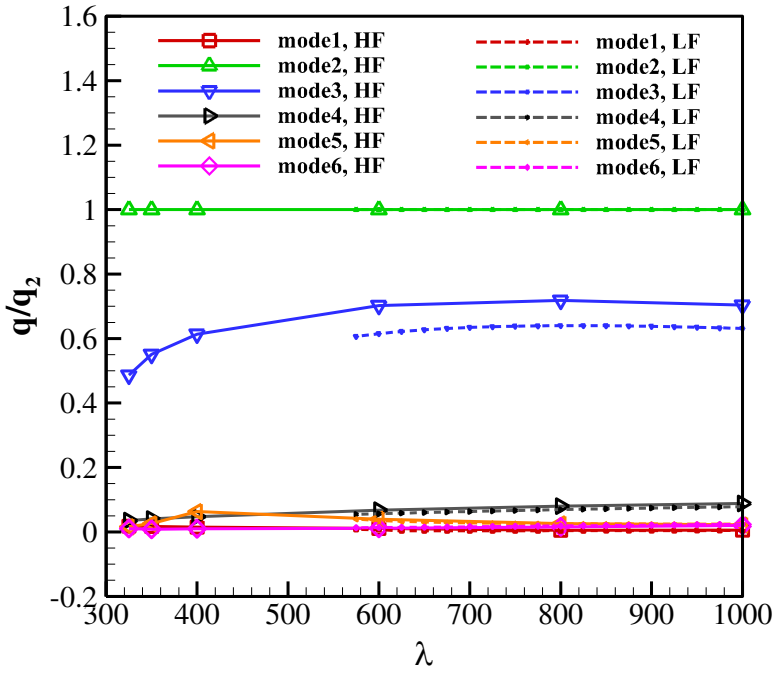

(a) xi/l=50%

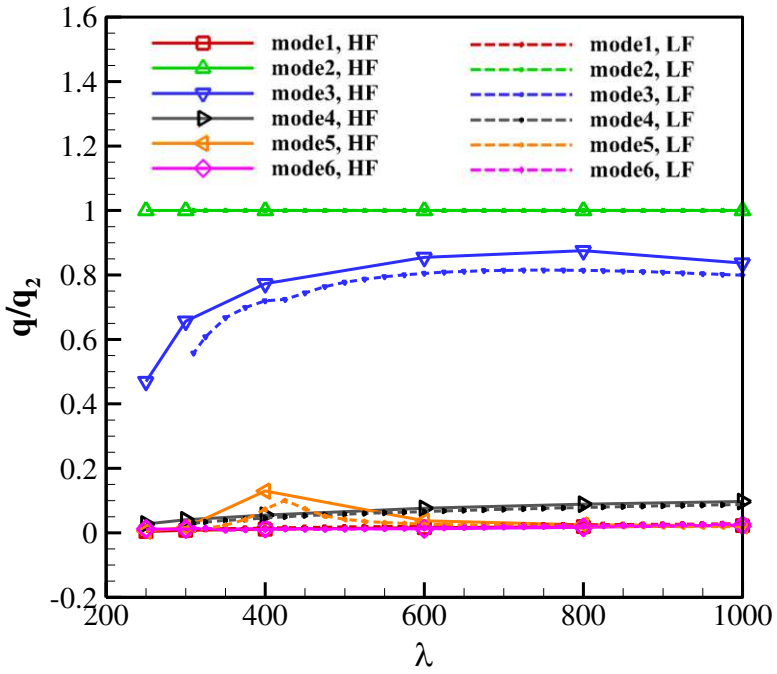

(b) xi/l=49%

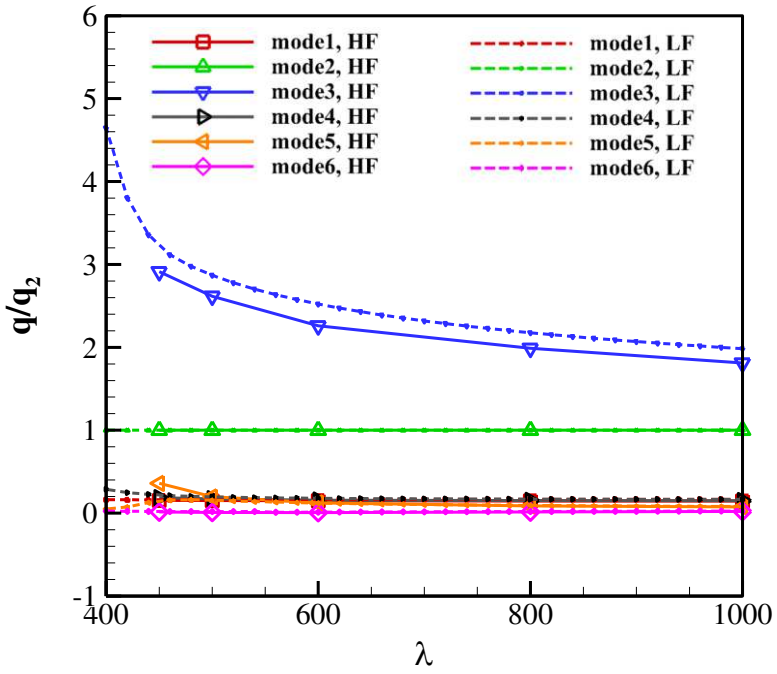

(c) xi/l=42%

Fig. 6 The modal participation for mode 1 through mode 6 with the variation of dynamic pressure, P3/P1=1.8, Ma=2.0

In order to examine the universality of the variation trend of system bifurcation characteristics, another set of simulations are carried out at P3/P1 = 1.4, where the system bifurcation type has been reported as a subcritical bifurcation in many literatures [9,24,50]. The results are shown in Fig. 7. It can be seen from the figures that the variation trend of bifurcation characteristics is very similar to that of P3/P1 = 1.4, and the results predicted by the two computational frameworks are still closely correlated. As the shock impingement point moves forward, the bifurcation type transitions from a subcritical bifurcation to a supercritical bifurcation, with continuously increasing LCO frequencies and continuously decreasing LCO amplitudes. Meanwhile, the bifurcation point gradually moves forward and then moves backward when it reaches its minimum value.

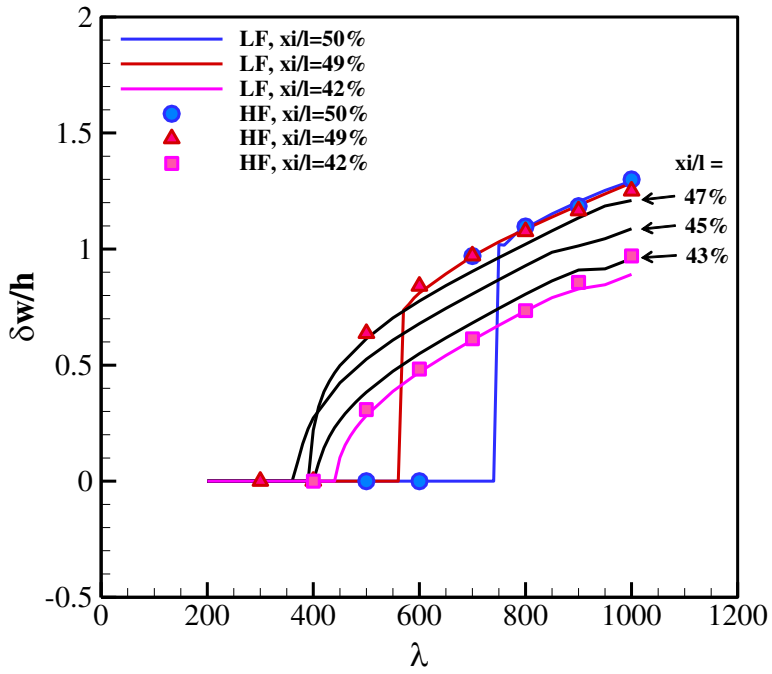

(a) LCO amplitude at 75% chord length

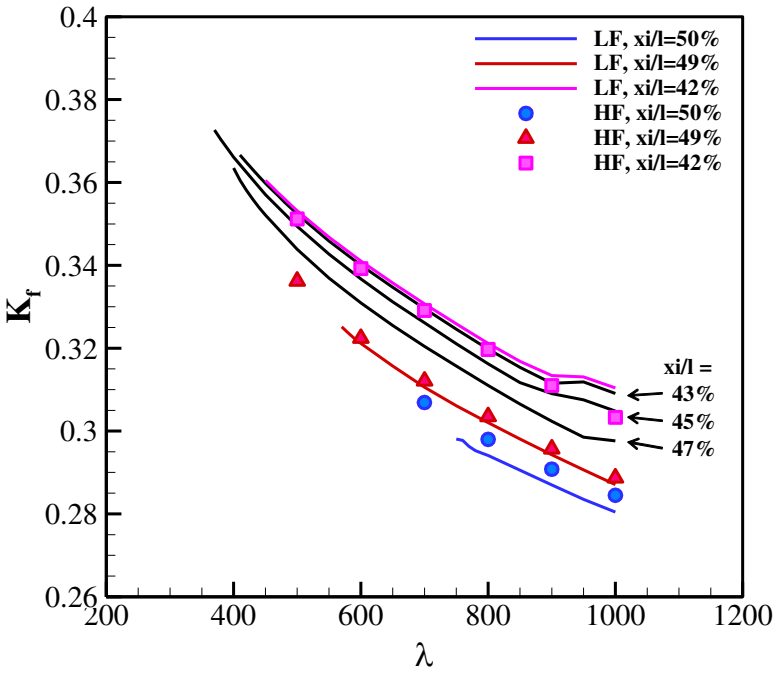

(b) Dominant LCO frequency at 75% chord length

Fig. 7 Effects of the impingement location on the LCOs, P3/P1=1.4, Ma=2.0

The modal participation for the shock impingement locations of x_i/l=50%, 49% and 42% are shown in Fig. 8(a-c). As can be seen from these figures, in addition to the second and third modes with relatively high proportion, the proportion of the fifth mode gradually increases with the increase of the non-dimensional dynamic pressure. Noted that the two computational frameworks can predict similar modal participation variation trends for the shock impingement locations of x_i/l=50% and x_i/l=49%. However, for the shock impingement locations of x_i/l=42%., the low-fidelity framework fails to predict the continuous growth trend of the fifth mode. This explains the differences in LCO characteristics predicted by the two computational frameworks in Fig. 7.in the range of λ=880~1000.

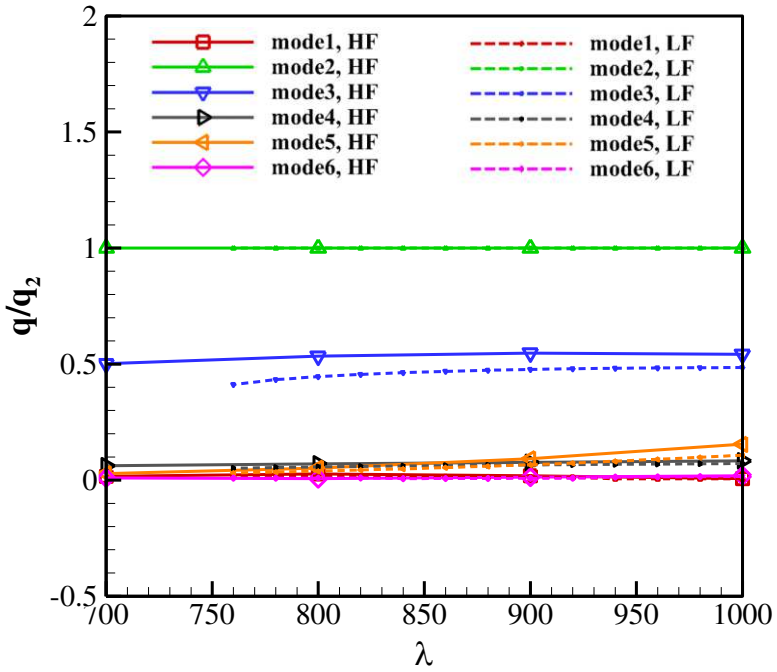

(a) xi/l=50%

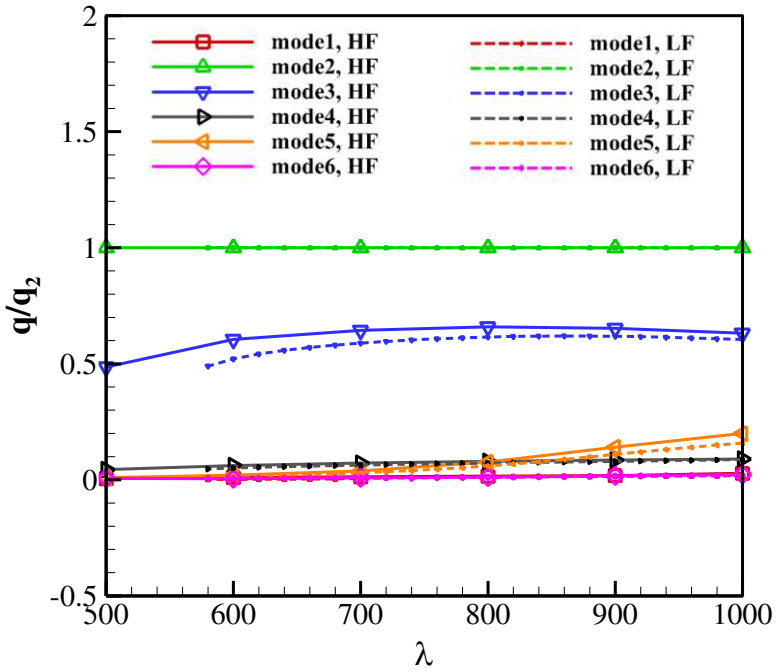

(b) xi/l=49%

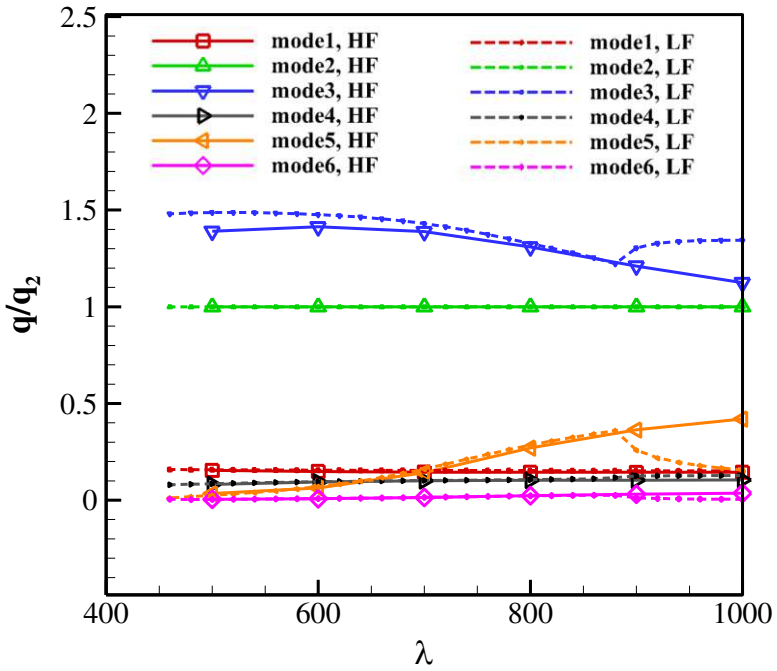

(c) xi/l=42%

Fig. 8 The modal participation for mode 1 through mode 6 with the variation of dynamic pressure, P3/P1=1.4, Ma=2.0

3.3 Effect of the cavity pressure

In this section, the effects of the cavity pressure on the bifurcation characteristics are investigated. Defining the cavity pressure ratio as $P_c = p_c / p_\infty$. A set of simulations are carried out at different cavity pressure ratios, and a summary of all computations for cases of P3/P1=1.8 is given in Fig. 9. As shown in Fig. 9, the variation trend of system bifurcation characteristics with the cavity pressure is very similar to that with the shock impingement location. In Fig. 9 (a), at first, the bifurcation point moves to the left as the cavity pressure increases, and then starts to move to the right when it reaches its minimum value. Meanwhile, the aeroelastic system gradually transitions from a subcritical bifurcation to a supercritical bifurcation. For a given λ, as the cavity pressure increases, the LCO amplitude decreases continuously while the LCO frequency increases gradually. Noted that the

accuracy of the low-fidelity framework for predicting the LCO amplitude decreases significantly when the cavity pressure ratio P_c is increased to 1.48. This should be caused by the curvature effect of the statically deformed panel under high cavity pressure, which leads to a reduction of the accuracy of local piston theory.

Fig. 10(a) and (b) show the modal participation variation with λ for cavity pressure ratios of 1.44 and 1.48, respectively. As can be seen from the figures, the proportion of the second and third modes is much higher than that of the other modes, and the variation trend of the modal participation is also similar to that of Fig. 6(a) and (b). For a given λ, the proportion of the third mode increases as the cavity pressure increases. It can be expected that if the cavity pressure continues to increase, the proportion of the third mode will exceed that of the second mode as shown in Fig. 6(c). In addition, the proportion of third modes predicted by the low-fidelity framework is obviously lower than that predicted by the high-fidelity framework, which corresponds to the differences in the LCO amplitudes predicted by the two computational frameworks.

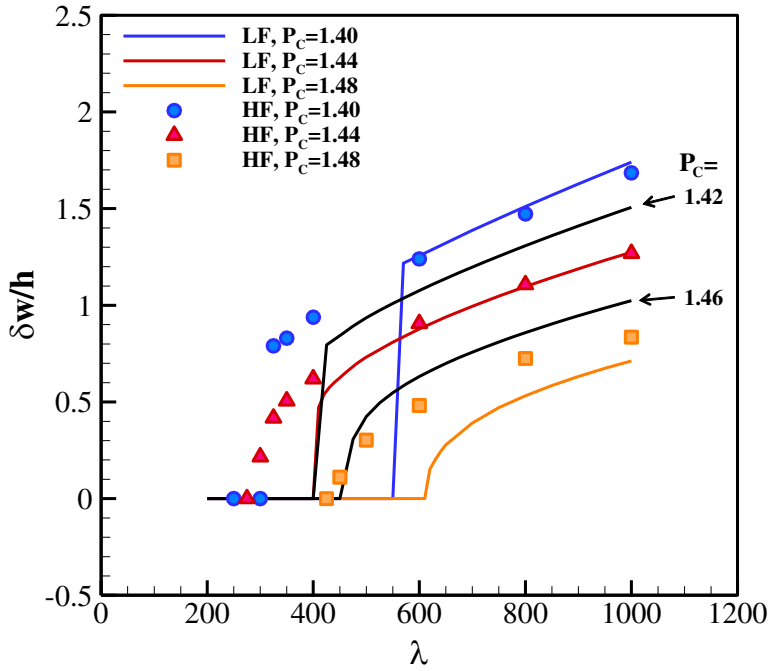

(a) LCO amplitude at 75% chord length

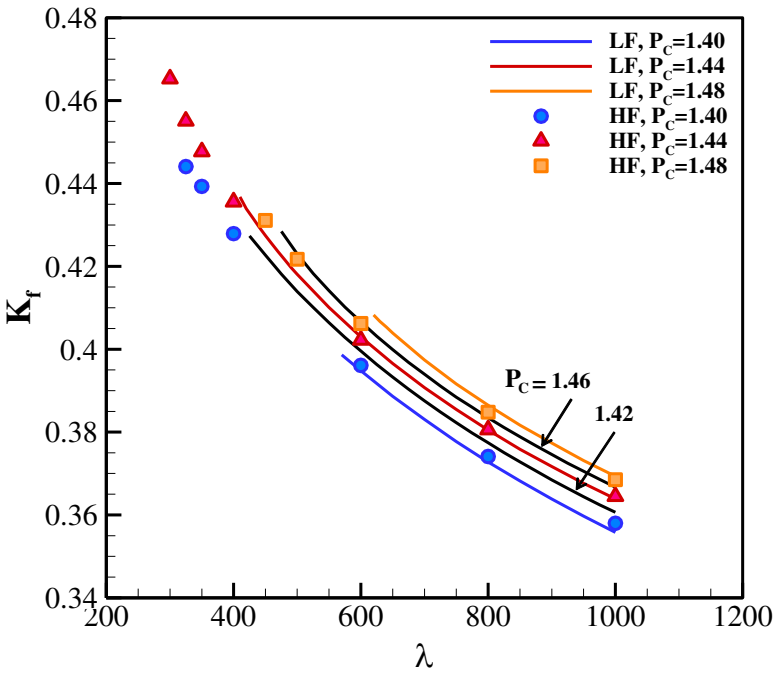

(b) Dominant LCO frequency at 75% chord length

Fig. 9 Effects of the cavity pressure on the LCOs at Mach 2,0, P3/P1=1.8, x_i/l =50%, Ma=2.0

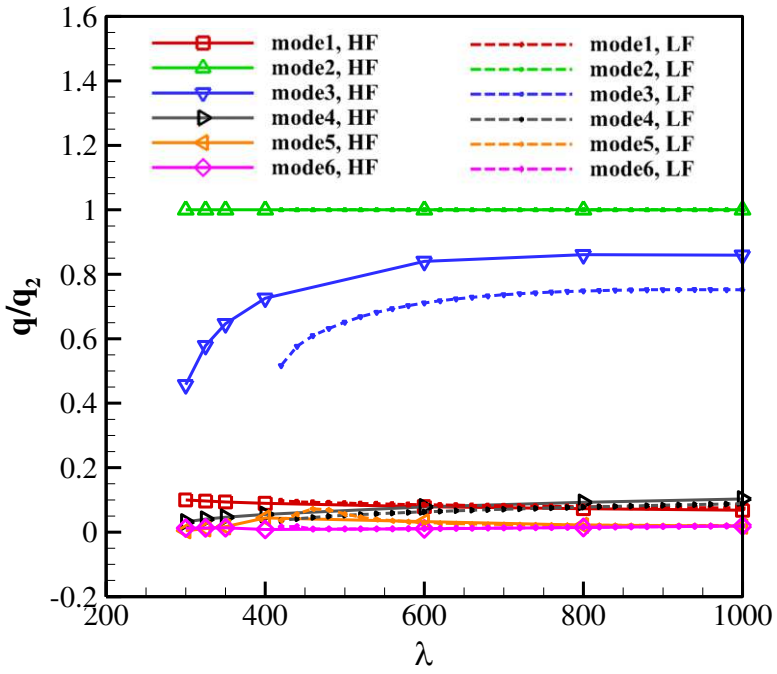

(a) P_C = 1.44

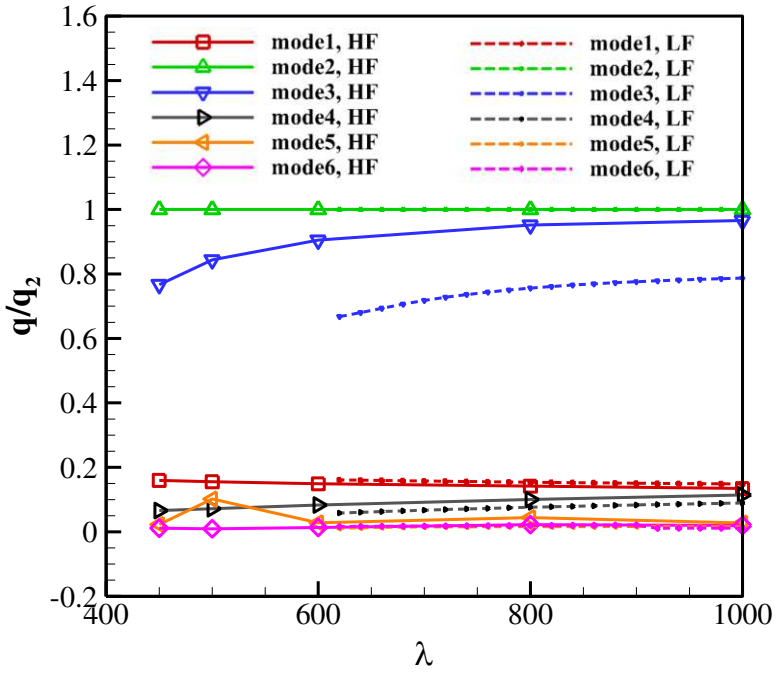

(b) P_C = 1.48

Fig. 10 The modal participation for mode 1 through mode 6 with the variation of dynamic pressure, P3/P1=1.8, x_i/l =50%, Ma=2.0

Fig. 11 shows the collection of cases for P3/P1=1.4. The shock impingement point is placed at x_i/l=49%. This is because that for the impingement location of x_i/l=50%, only the fixed points are obtained for P_c >1.2 within the studied non-dimensional dynamic pressure range._In Fig. 11(a), the system has a clear tendency to gradually transition from a subcritical bifurcation to a supercritical bifurcation as the cavity pressure increases, which is constant with that shown in Fig. 9. The difference is that within the current parameter range, the bifurcation point only moves to the right as cavity pressure increases. In Fig. 11(b), the LCO frequency increases as the cavity pressure ratio increases. The variation of modal participation is shown in Fig. 12, which has the same characteristics as that of Fig. 8(a) and (b). The second and third mode still have a higher proportion than other modes, and the fifth mode has a clear growth trend as the non-dimensional dynamic pressure increases.

The above calculation results show that the bifurcation characteristics of the system have similar variation trends when changing the back pressure and the shock impingement location, which indicates that these phenomena may have the same underlying mechanism.

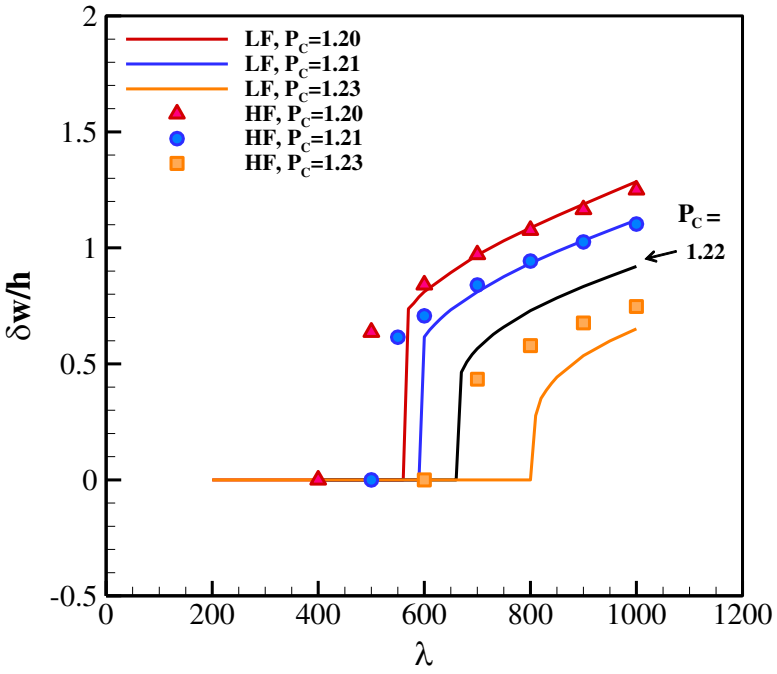

(a) LCO amplitude at 75% chord length

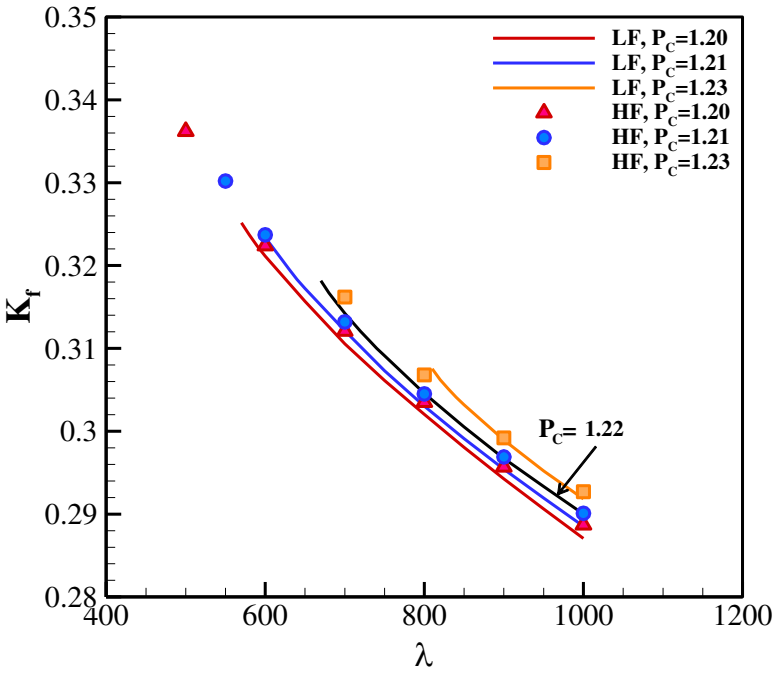

(b) Dominant LCO frequency at 75% chord length

Fig. 11 Effects of the cavity pressure on the LCOs at Mach 2,0, P3/P1=1.4, x_i/l =49%, Ma=2.0

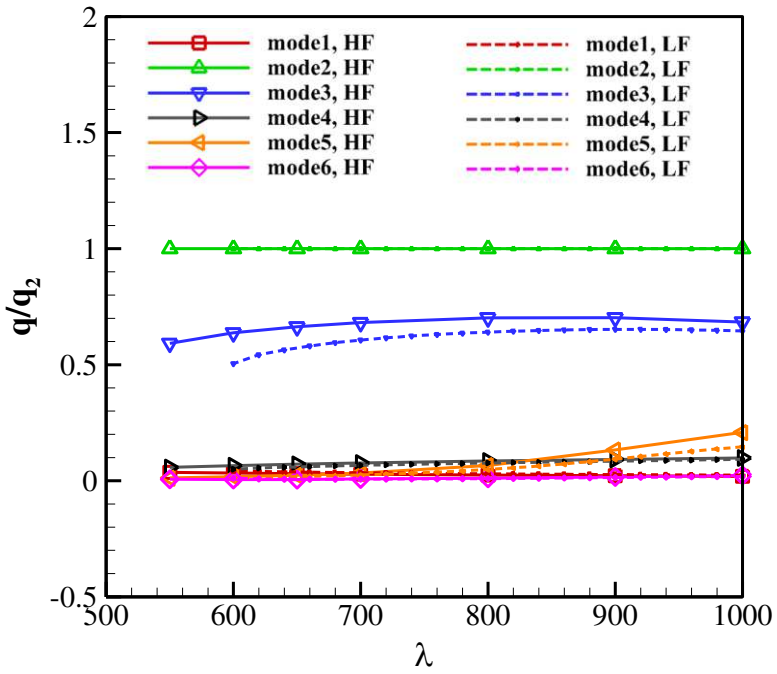

(a) P_C = 1.21

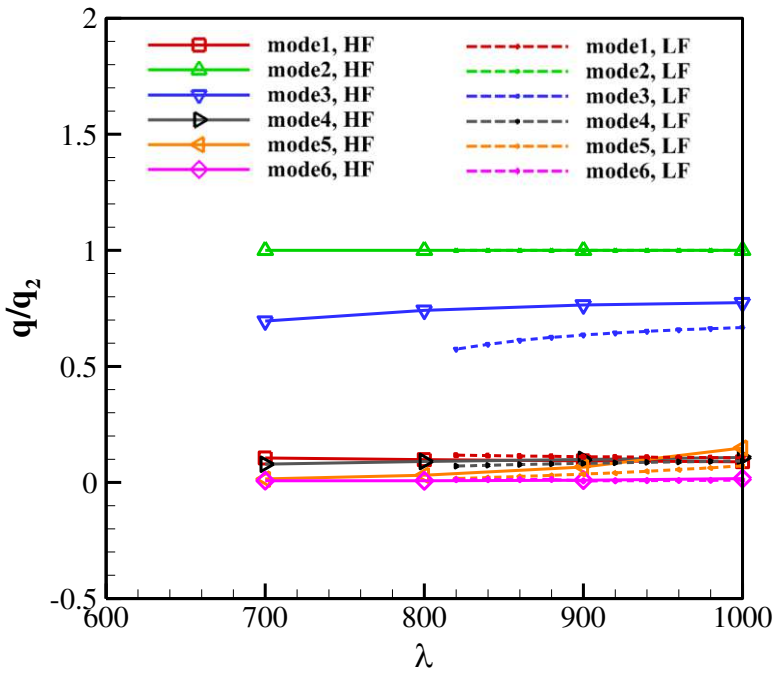

(b) P_C = 1.23

Fig. 12 The modal participation for mode 1 through mode 6 with the variation of dynamic pressure, P3/P1=1.4, x_i/l =49%, Ma=2.0

3.4 Effect of the initial condition

The effect of the initial condition is the last item discussed in this study. It is known that for many nonlinear systems, the system dynamic behaviors can be affected by the initial conditions. In previous studies [9,10,24,50] have pointed out that for some shock impingement conditions where the aeroelasticity system shows the features of a subcritical bifurcation, the system dynamic responses can be led into two different states, a fixed point and a stable LCO. Almost all LCOs were reported in the form of a combination of the second and third mode. However, in this section, it will be shown that multiple stable LCOs exist for the current aeroelastic system, and that these LCOs can be triggered by proper initial conditions.

In order to investigate the effects of initial condition, the velocity perturbations in the form of first to sixth mode with different magnitudes are used to excite the system from a static aeroelastic equilibrium state. The low-fidelity framework is adopted here to conduct an exploratory study. The simulations are carried out at P3/P1=1.8 with λ=1000, x_i/l=49%. Long time of fluid-structure interaction simulations are used to obtain the stable LCOs amplitudes and peak frequencies at x/l=75%. The results are summarized in Fig. 13.

In Fig. 13, each type of symbol in specific color represents a time domain simulation initiated by a corresponding modal velocity perturbation. In the current case, the 3rd mode velocity perturbation can excite a LCO starting from the minimum magnitude of 100. As the perturbation magnitude increases to 600, another stable LCO with higher amplitude and higher frequency is excited. For the velocity perturbation of other modes, larger magnitudes are required to excite the LCOs. According to the amplitude diagram and peak frequency diagram shown in Fig. 13, about six stable LCOs have been excited by different types initial conditions. The LCO with lowest non-zero frequency corresponds to that discussed in Section 3.2 and 3.3. The results here show that this type of LCO can also be excited by the 2nd, 3rd and

4th mode velocity perturbation. The LCOs with other frequencies have rarely been reported in literatures. For these LCOs, coupling occurs between higher order modes, and the LCOs excited by velocity perturbations of higher modes tend to have higher frequencies.

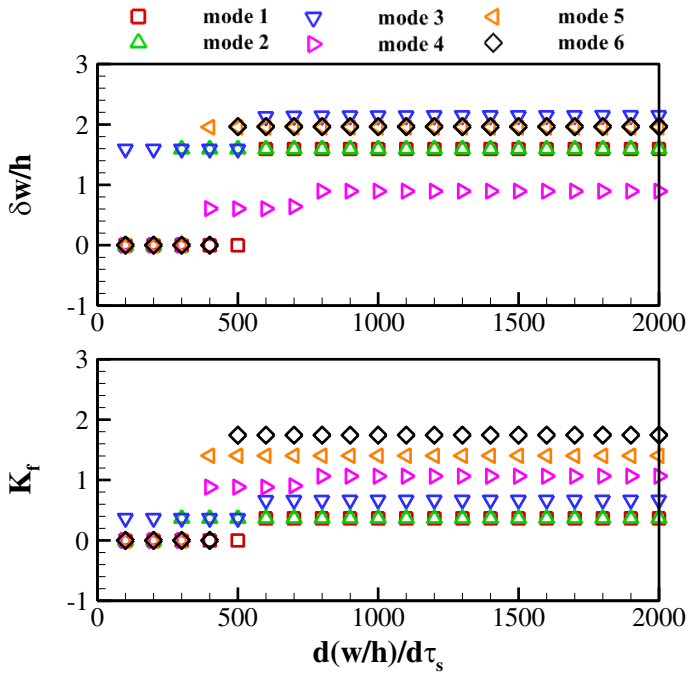

Fig. 13 Effects of the initial condition on the LCO amplitude at 75% chord length, Ma=2.0, P3/P1=1.8, λ=1000, x_i/l=49%

Fig. 14 and Fig. 15 shows the modal participation of LCOs on several states of Fig. 13. The verifications by the high-fidelity framework are also provided. Fig. 14 shows LCO time domain responses initiated by the third mode velocity perturbation. It can be seen from the figures that the third mode and fourth mode have a much higher proportion than other modes, which indicates the coupling between the two modes. In Fig. 15, the LCO time domain responses are initiated by the fourth mode velocity perturbation, which leads to a coupling between fourth and fifth mode. Fig. 14(c) and Fig. 15(c) show that the modal participation predicted by the high-fidelity framework agrees well with that predicted by the low-fidelity framework, which verifies the drawn conclusions. Additional comparison between the frequency

contents of the LCOs predicted by the two computational frameworks are shown in Fig. 16. Despite the slight offset in the higher frequency contents, the peaks frequencies agree well each other, which further adds credibility to the current conclusions.

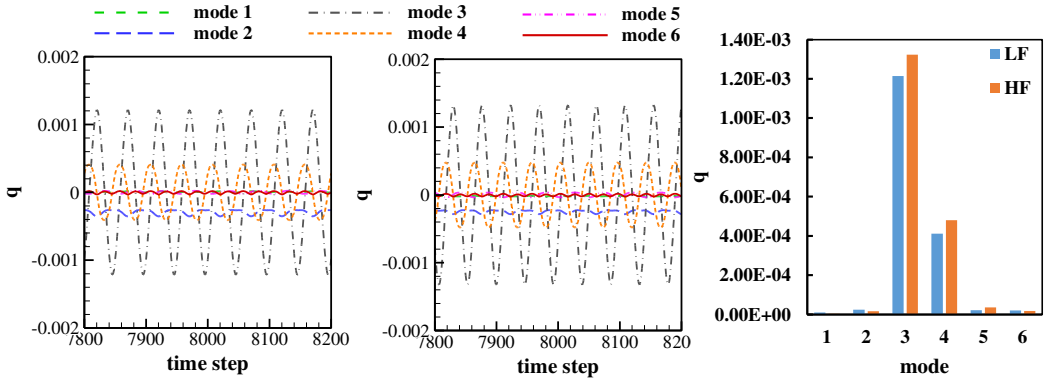

(a) LF (b) HF (c) modal amplitude

Fig. 14 Time domain responses, initiated by 3rd mode velocity perturbation of $d(w/h)/d\tau_s = 1000$, P3/P1=1.8, λ=1000, x_i/l=49%, Ma=2.0

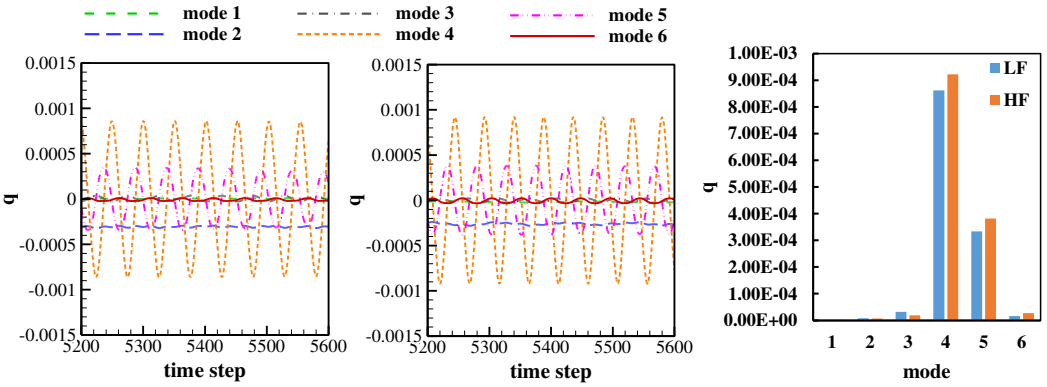

(a) LF (b) HF (c) modal amplitude

Fig. 15 Time domain responses, initiated by 4th mode velocity perturbation of $d(w/h)/d\tau_s = 1000$, P3/P1=1.8, λ=1000, x_i/l=49%, Ma=2.0

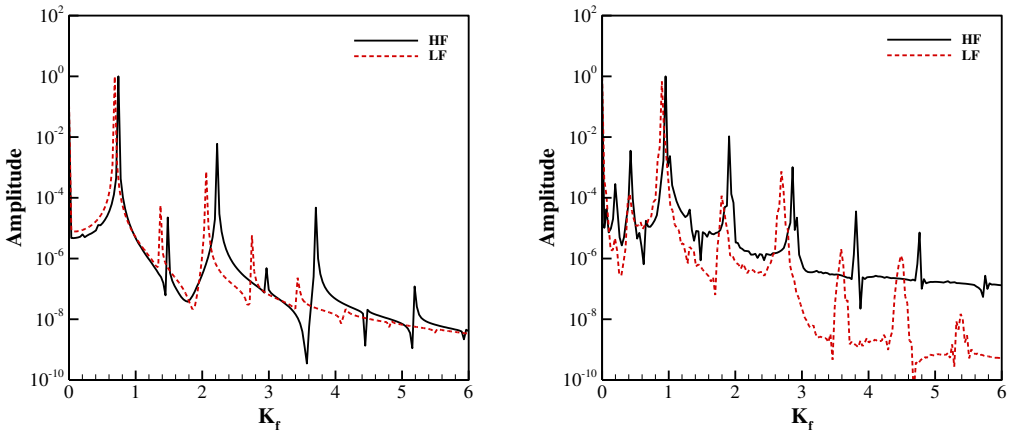

(a) 3rd mode velocity disturbance (b) 4th mode velocity disturbance

Fig. 16 Fourier analysis of LCO at x/l =75%, initiated by different mode velocity perturbation of $d(w/h)/d\tau_s = 1000$, P3/P1=1.8, λ =1000, x_i/l =49%, Ma=2.0

Investigating further, the instantaneous flow field is extracted to provide a more intuitive view on these LCOs. Fig. 17(a) and Fig. 17(b) show the instantaneous flow fields extracted from the time domain responses initiated by the third and fourth mode velocity perturbations, respectively. The wall boundary shown in Fig. 17(a) exhibits a deformation in the form of an approximate of third mode shape, while that of Fig. 17(b) exhibits a deformation in the form of an approximate of fourth mode shape. The deformation of wall introduces additional compression and expansion waves to the flow field. Moreover, the deformation in the higher mode shape tends to introduce more of these waves, presenting a higher frequency of recompression/expansion near the panel trailing edge. These phenomena can cause more severe pressure fluctuations on the surrounding structure, thus increasing the risk of structural fatigue failure.

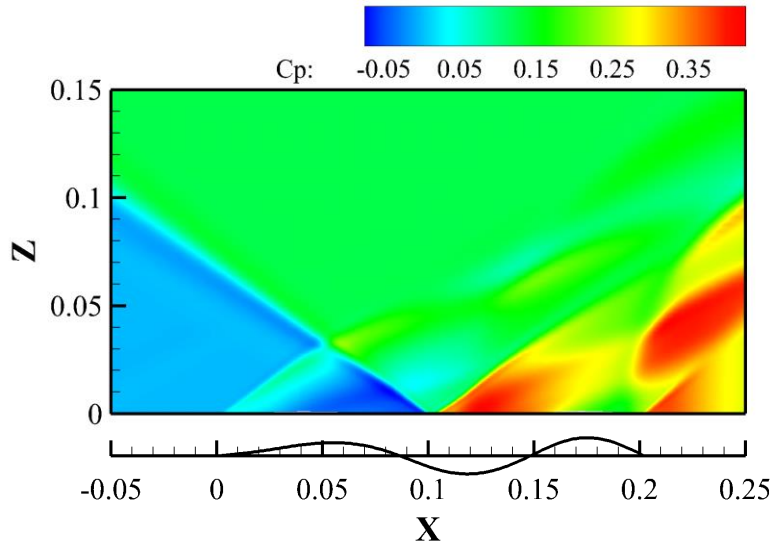

(a) Initiated by 3rd mode velocity disturbance

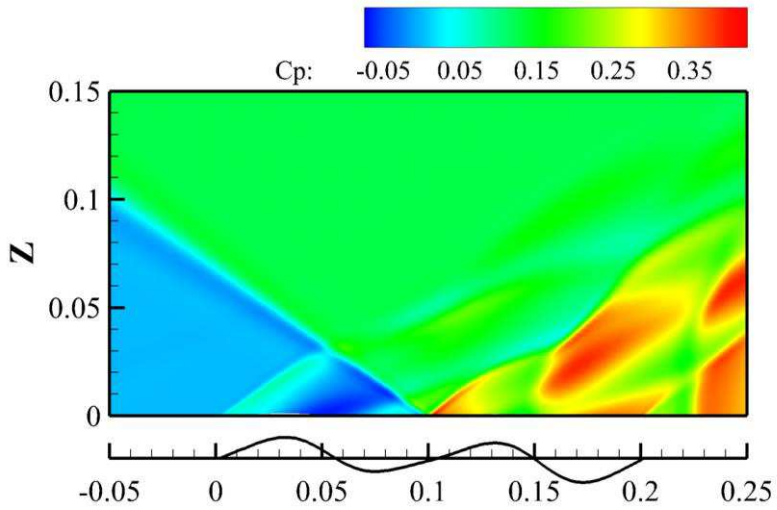

(b) Initiated by 4th mode velocity disturbance

Fig. 17 Instantaneous flow field at Ma=2.0, P3/P1=1.8, λ=1000, x_i/l=49%

It is worth of mentioning that, similar multiple LCOs phenomena have ever been observed in our previous studies on the classic panel flutter at low supersonic speed [40] (see Fig. 16 of this reference). Recently, Shishaeva et al. [51] has also studied the effect of external perturbations on nonlinear panel flutter at low supersonic speed. It is found that depending on the initial perturbation, different LCOs can be developed, which should be the same phenomenon that predicted by the reduced order model in our previous work [40]. The current phenomena of multiple LCOs in the shock induced panel flutter share many common features with those of Ref. [40] and Ref.

[51]， and it will be of particular interest to reveal the underlying mechanisms of these nonlinear phenomena in future studies.

4. Conclusions

For a two-dimensional elastic panel subjected to an inviscid impinging oblique shock wave, the effects of the shock impingement location, cavity pressure and initial condition on the bifurcation characteristics and dynamic behaviors of the aeroelastic system are investigated numerically. Several interesting phenomena are observed in the fluid-structure interaction simulations using the low-fidelity numerical method and then confirmed by the high-fidelity CFD/CSD coupling method. The main conclusions are surmised as follows.

First, it is observed that as the impingement point moves from the midpoint of the elastic panel to the leading edge, the system gradually transitions from a subcritical bifurcation to a supercritical bifurcation with a continuously decreasing LCO amplitude and increasing LCO frequency. Meanwhile, the bifurcation point moves to the direction corresponds to smaller value of dynamic pressure and then moves backward when the impingement point surpass a critical position. For the cases where the impingement point is near the center of the elastic panel, the aeroelastic system exhibits strong sensitive to the shock impingement location, e.g., even a 1% shift in panel length could induce significant changes in bifurcation point or even changes in bifurcation type.

Second, the effects of cavity pressure on the bifurcation characteristics of the aeroelastic system are quite similar to that of shock impingement location. As the cavity pressure increases, the system experiences a gradual transition from a subcritical bifurcation to a supercritical bifurcation, while the LCO amplitude decreases and LCO frequency increases. The variation of the bifurcation point with the cavity pressure is also similar to that of the shock impingement point, and there

exist a minimum value of non-dimensional dynamic pressure corresponds to the bifurcation point when changing the cavity pressure.

Finally, in addition to the single LCO in the form of a combination of the second and third structural modes, multiple stable LCOs due to the coupling of higher order modes exist for the a given flow condition. These LCOs have high frequencies and can be developed when the structural modal velocity perturbations with high magnitudes or in the form of higher order modes are applied. Moreover, some of these LCOs even have higher amplitudes compared to the LCOs due to the coupling between the second and third mode. Besides, those LCOs excited by velocity perturbations of higher-order modes are observed to be characterized by the coupling between the excited mode and its adjacent higher-order mode.

The results of present study show that either the shock impingement location or the cavity can induce the aeroelastic system to transition between a subcritical bifurcation and a supercritical bifurcation, which suggest two additional potential approaches for the bifurcation type control of shock induced panel flutter. However, limited by the content and intentions of this paper, the combined effects of the two approaches are left for future studies. Besides, the observed higher-order mode coupled LCOs are more dangerous for the structure integrity due to its high frequency and amplitudes, and should be further studied in future research work.

Appendix. Validation of FSI coupling method

A two-dimensional case of classic panel flutter from Ref. [52] is used for validating the fluid-structure coupling method. The computational domain and the results are shown in Fig. 18. It can be seen from the figure that the flutter boundary predicted by the high-fidelity framework matches closely with the linear stability analysis results in Ref. [52], and also have a good correlation with those from other literatures [53-55]. For Ma>1.7, where piston theory is applicable, the flutter

boundary predicted by the low-fidelity framework correlated well with that predicted by the high-fidelity framework. To validate the solver's ability for predicting nonlinear responses, the LCOs at Ma=2.0 are calculated and the results are shown in Fig. 19. The predicted LCO amplitudes and peak frequencies agree well with that of Ref. [9]. All these should have validated the developed FSI procedure and solver implementation, providing confidence for this study.

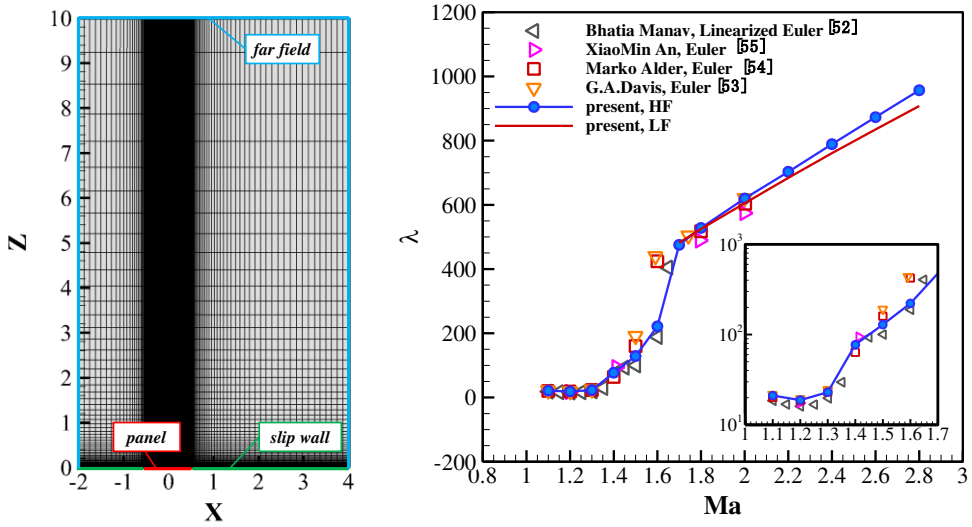

(a) Computational domain (b) flutter boundary

Fig. 18 Computational domain and flutter for a two-dimensional simply supported panel $h/l=0.002$, $\mu=0.1$

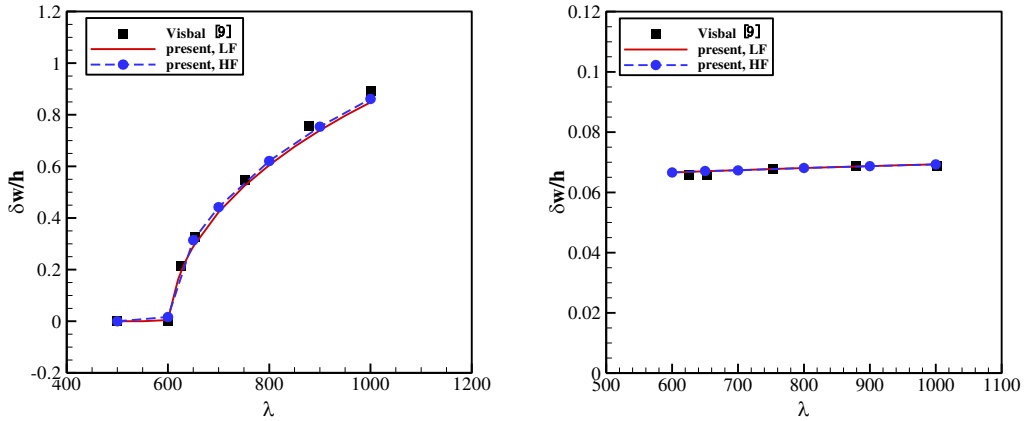

(a) LCO amplitude (b) LCO peak frequency

Fig. 19 LCOs at Ma=2.0, $h/l=0.002$, $\mu=0.1$

Statements and Declarations

Acknowledgements

This study is supported by the National Natural Science Foundation of China (No. U2141254, No. 92052109).

Competing Interests

The authors have no relevant financial or non-financial interests to disclose.

Data Availability Statement

Data will be available on reasonable request

Reference

[1] Miller, B., Crowell, A., and McNamara, J. Modeling and Analysis of Shock Impingements on Thermo-Mechanically Compliant Surface Panels. In *53rd AIAA/ASME/ASCE/AHS/ASC Structures, Structural Dynamics and Materials Conference*, American Institute of Aeronautics and Astronautics, 2012.

[2] Beberniss, T., Spottswood, M., and Eason, T. High-Speed Digital Image Correlation Measurements of Random Nonlinear Dynamic Response BT - Experimental and Applied Mechanics, Volume 6. 2011.

[3] Michael Spottswood, S., Beberniss, T. J., Eason, T. G., Spottswood, S. M., Eason, T. G., Beberniss, T. J., Michael Spottswood, S., Beberniss, T. J., and Eason, T. G. "Full-Field, Dynamic Pressure and Displacement Measurements of a Panel Excited by Shock Boundary-Layer Interaction." *19th AIAA/CEAS Aeroacoustics Conference*, 2013, p. 15. https://doi.org/10.2514/6.2013-2016.

[4] Willems, S., Gülhan, A., and Esser, B. "Shock Induced Fluid-Structure Interaction on a Flexible Wall in Supersonic Turbulent Flow." Vol. 5, 2013, pp. 285–308. https://doi.org/10.1051/eucass/201305285.

[5] Pasquariello, V., Hickel, S., Adams, N. A., Hammerl, G., Wall, W. A., Daub, D., Willems, S., and Gülhan, A. Coupled Simulation of Shock-Wave/Turbulent Boundary-Layer Interaction over a Flexible Panel. 2015.

[6] Daub, D., Willems, S., and Gülhan, A. "Experimental Results on Unsteady

Shock-Wave/Boundary-Layer Interaction Induced by an Impinging Shock." *CEAS Space Journal*, Vol. 8, No. 1, 2016, pp. 3–12. https://doi.org/10.1007/s12567-015-0102-4.

[7] Daub, D., Willems, S., and Gülhan, A. "Experiments on the Interaction of a Fast-Moving Shock with an Elastic Panel." *AIAA Journal*, Vol. 54, No. 2, 2015, pp. 670–678. https://doi.org/10.2514/1.J054233.

[8] Gogulapati, A., Deshmukh, R., Crowell, A. R., McNamara, J. J., Vyas, V., Wang, X., and Mignolet, M. P. Response of a Panel to Shock Impingement: Modeling and Comparison with Experiments. In *55th AIAA/ASME/ASCE/AHS/ASC Structures, Structural Dynamics, and Materials Conference*, American Institute of Aeronautics and Astronautics, 2014.

[9] Visbal, M. R. "On the Interaction of an Oblique Shock with a Flexible Panel." *Journal of Fluids and Structures*, Vol. 30, 2012, pp. 219–225. https://doi.org/https://doi.org/10.1016/j.jfluidstructs.2012.02.002.

[10] Visbal, M. R. "Viscous and Inviscid Interactions of an Oblique Shock with a Flexible Panel." *Journal of Fluids and Structures*, Vol. 48, 2014, pp. 27–45. https://doi.org/https://doi.org/10.1016/j.jfluidstructs.2014.02.003.

[11] Shahriar, A., Shoele, K., and Kumar, R. Aero-Thermo-Elastic Simulation of Shock-Boundary Layer Interaction over a Compliant Surface. In *2018 Fluid Dynamics Conference*, American Institute of Aeronautics and Astronautics, 2018.

[12] Boyer, N. R., McNamara, J. J., Gaitonde, D. V, Barnes, C. J., and Visbal, M. R. "Features of Shock-Induced Panel Flutter in Three-Dimensional Inviscid Flow." *Journal of Fluids and Structures*, Vol. 83, 2018, pp. 490–506. https://doi.org/https://doi.org/10.1016/j.jfluidstructs.2018.10.001.

[13] Shinde, V., McNamara, J., Gaitonde, D., Barnes, C., and Visbal, M. "Transitional Shock Wave Boundary Layer Interaction over a Flexible Panel." *Journal of Fluids and Structures*, Vol. 90, 2019, pp. 263–285. https://doi.org/https://doi.org/10.1016/j.jfluidstructs.2019.07.007.

[14] Shinde, V. J., McNamara, J. J., and Gaitonde, D. V. Effect of Structural Parameters on Shock Wave Boundary Layer Induced Panel Flutter. In *AIAA Aviation 2019 Forum*, American Institute of Aeronautics and Astronautics, 2019.

[15] Varigonda, S. V., and Narayanaswamy, V. Investigation of Shock Wave Oscillations over a Flexible Panel in Supersonic Flows. In *AIAA Aviation 2019 Forum*, American Institute of Aeronautics and Astronautics, 2019.

[16] Peltier, S. J., Rice, B. E., Szmodis, J., Ogg, D. R., Hofferth, J. W., Sellers, M. E., and Harris, A. J. Aerodynamic Response to a Compliant Panel in Mach 4 Flow. In *AIAA Aviation 2019 Forum*, American Institute of Aeronautics and Astronautics, 2019.

[17] Spottswood, S. M., Beberniss, T. J., Eason, T. G., Perez, R. A., Donbar, J. M., Ehrhardt, D. A., and Riley, Z. B. "Exploring the Response of a Thin, Flexible

Panel to Shock-Turbulent Boundary-Layer Interactions." *Journal of Sound and Vibration*, Vol. 443, 2019, pp. 74–89. https://doi.org/https://doi.org/10.1016/j.jsv.2018.11.035.

[18] Tripathi, A., Gustavsson, J., Shoele, K., and Kumar, R. Response of a Compliant Panel to Shock Boundary Layer Interaction at Mach 2. In *AIAA Scitech 2021 Forum*, American Institute of Aeronautics and Astronautics, 2021.

[19] Tripathi, A., Gustavsson, J., Shoele, K., and Kumar, R. Effect of Shock Impingement Location on the Fluid-Structure Interaction over a Compliant Panel. In *AIAA SCITECH 2022 Forum*, American Institute of Aeronautics and Astronautics, 2021.

[20] Daub, D., Willems, S., and Gülhan, A. "Experiments on Aerothermoelastic Fluid–Structure Interaction in Hypersonic Flow." *Journal of Sound and Vibration*, Vol. 531, 2022, p. 116714. https://doi.org/https://doi.org/10.1016/j.jsv.2021.116714.

[21] Shinde, V. J., McNamara, J. J., and Gaitonde, D. V. Shock Wave Turbulent Boundary Layer Interaction Over a Flexible Panel. In *AIAA Scitech 2021 Forum*, American Institute of Aeronautics and Astronautics, 2021.

[22] Zope, A., Horner, C., Collins, E. M., Bhushan, S., and Bhatia, M. Investigation of Flexible Panel Dynamic Response Induced by Coherent Turbulent Vortical Structures. In *AIAA Scitech 2021 Forum*, American Institute of Aeronautics and Astronautics, 2021.

[23] Gogulapati, A., Deshmukh, R., McNamara, J. J., Vyas, V., Wang, X. Q., Mignolet, M., Beberniss, T., Spottswood, S. M., and Eason, T. G. "Response of a Panel to Shock Impingement: Modeling and Comparison with Experiments - Part 2." *56th AIAA/ASCE/AHS/ASC Structures, Structural Dynamics, and Materials Conference*, No. January, 2015, pp. 1–23. https://doi.org/10.2514/6.2015-0685.

[24] Brouwer, K. R., and McNamara, J. J. "Enriched Piston Theory for Expedient Aeroelastic Loads Prediction in the Presence of Shock Impingements." *AIAA Journal*, Vol. 57, No. 3, 2019, pp. 1288–1302. https://doi.org/10.2514/1.J057595.

[25] Brouwer, K. R., and McNamara, J. J. "Surrogate-Based Aeroelastic Loads Prediction in the Presence of Shock-Induced Separation." *Journal of Fluids and Structures*, Vol. 93, 2020, p. 102838. https://doi.org/https://doi.org/10.1016/j.jfluidstructs.2019.102838.

[26] Brouwer, K. R., Perez, R. A., Beberniss, T. J., Spottswood, S. M., and Ehrhardt, D. A. "Evaluation of Reduced-Order Aeroelastic Simulations for Shock-Dominated Flows." *Journal of Fluids and Structures*, Vol. 108, 2022, p. 103429. https://doi.org/https://doi.org/10.1016/j.jfluidstructs.2021.103429.

[27] Ye, L.-Q., and Ye, Z.-Y. "Effects of Shock Location on Aeroelastic Stability of Flexible Panel." *AIAA Journal*, Vol. 56, No. 9, 2018, pp. 3732–3744.

https://doi.org/10.2514/1.J056924.

[28] Ye, L., Ye, Z., Ye, K., and Wu, J. “Aeroelastic Stability and Nonlinear Flutter Analysis of Viscoelastic Heated Panel in Shock-Dominated Flows.” *Aerospace Science and Technology*, Vol. 117, 2021, p. 106909. https://doi.org/https://doi.org/10.1016/j.ast.2021.106909.

[29] Ye, L., Ye, Z., Ye, K., and Wu, J. “Aeroelastic Stability Analysis of a Flexible Panel Subjected to an Oblique Shock Based on an Analytical Model.” *Acta Mechanica*, Vol. 232, No. 9, 2021, pp. 3539–3564. https://doi.org/10.1007/s00707-021-03023-3.

[30] Jonsson, E., Riso, C., Lupp, C. A., Cesnik, C. E. S., Martins, J. R. R. A., and Epureanu, B. I. “Flutter and Post-Flutter Constraints in Aircraft Design Optimization.” *Progress in Aerospace Sciences*, Vol. 109, 2019, p. 100537. https://doi.org/https://doi.org/10.1016/j.paerosci.2019.04.001.

[31] Guo, H., and Chen, Y. “Supercritical and Subcritical Hopf Bifurcation and Limit Cycle Oscillations of an Airfoil with Cubic Nonlinearity in Supersonic\hypersonic Flow.” *Nonlinear Dynamics*, Vol. 67, No. 4, 2012, pp. 2637–2649. https://doi.org/10.1007/s11071-011-0177-1.

[32] Li, P., Yang, Y., and Chen, G. “Analysis of Nonlinear Limit Cycle Flutter of a Restrained Plate Induced by Subsonic Flow.” *Nonlinear Dynamics*, Vol. 79, No. 1, 2015, pp. 119–138. https://doi.org/10.1007/s11071-014-1650-4.

[33] Iannelli, A., Lowenberg, M., and Marcos, A. “On the Effect of Model Uncertainty on the Hopf Bifurcation of Aeroelastic Systems.” *Nonlinear Dynamics*, Vol. 103, No. 2, 2021, pp. 1453–1473. https://doi.org/10.1007/s11071-020-06169-2.

[34] Boyer, N. R., McNamara, J. J., Gaitonde, D. V., Barnes, C. J., and Visbal, M. R. “Features of Shock-Induced Panel Flutter in Three-Dimensional Inviscid Flow.” *Journal of Fluids and Structures*, Vol. 83, 2018, pp. 490–506. https://doi.org/10.1016/j.jfluidstructs.2018.10.001.

[35] Meijer, M.-C., and Dala, L. “Generalized Formulation and Review of Piston Theory for Airfoils.” *AIAA Journal*, Vol. 54, No. 1, 2015, pp. 17–27. https://doi.org/10.2514/1.j054090.

[36] Van Dyke, M. “A Study of Second-Order Supersonic Flow Theory.” *NACA TR 1081*, 1951.

[37] Roe, P. L. Approximate Riemann Solvers, Parameter Vectors, and Difference Schemes. *Journal of Computational Physics*. 2. Volume 43, 357–372. https://www.engineeringvillage.com/share/document.url?mid=cpx_5931326&database=cpx. Accessed May 29, 2019.

[38] BARTH, T., and JESPERSEN, D. The Design and Application of Upwind Schemes on Unstructured Meshes. In *27th Aerospace Sciences Meeting*, American Institute of Aeronautics and Astronautics, 1989.

[39] Thomas, P. D., and Lombard, C. K. “Geometric Conservation Law and Its Application to Flow Computations on Moving Grids.” *AIAA Journal*, Vol. 17,

No. 10, 2008, pp. 1030–1037. https://doi.org/10.2514/3.61273.

[40] Zhou, H., Wang, G., Mian, H. H., and Qin, M. "Fluid-Structure Coupled Analysis of Tandem 2D Elastic Panels." *Aerospace Science and Technology*, Vol. 111, 2021, p. 106521. https://doi.org/10.1016/J.AST.2021.106521.

[41] Wang, G., Zhou, H., and Mian, H. H. "Numerical Analysis on Modal Stability Characteristics of 2D Panel Flutter at Low Supersonic Speeds." *Journal of Fluids and Structures*, Vol. 103, 2021, p. 103296. https://doi.org/10.1016/J.JFLUIDSTRUCTS.2021.103296.

[42] Dowell, E. H. "Nonlinear Oscillations of a Fluttering Plate. II." *AIAA Journal*, Vol. 4, No. 10, 1967, pp. 1856–1862. https://doi.org/10.2514/3.4316.

[43] Wittig, K. "CalculiX USER'S MANUAL-CalculiX GraphiX, Version 2.17." 2016.

[44] Abaqus, G. "Abaqus 6.11." *Dassault Systemes Simulia Corporation, Providence, RI, USA*, 2011.

[45] Hilber, H. M., Hughes, T. J. R., and Taylor, R. L. "Improved Numerical Dissipation for Time Integration Algorithms in Structural Dynamics." *Earthquake Engineering & Structural Dynamics*, Vol. 5, No. 3, 1977, pp. 283–292. https://doi.org/https://doi.org/10.1002/eqe.4290050306.

[46] Zhang, W., Jiang, Y., and Ye, Z. "Two Better Loosely Coupled Solution Algorithms of CFD Based Aeroelastic Simulation." *Engineering Applications of Computational Fluid Mechanics*, Vol. 1, No. 4, 2007, pp. 253–262. https://doi.org/10.1080/19942060.2007.11015197.

[47] Huang, D., Rokita, T., and Friedmann, P. P. "Integrated Aerothermoelastic Analysis Framework with Application to Skin Panels." *AIAA Journal*, Vol. 56, No. 11, 2018, pp. 4562–4581. https://doi.org/10.2514/1.J056677.

[48] Rendall, T., and Allen, C. An Efficient Fluid-Structure Interpolation and Mesh Motion Scheme for Large Aeroelastic Simulations. In *26th AIAA Applied Aerodynamics Conference*, American Institute of Aeronautics and Astronautics, 2008.

[49] Wang, G., Chen, X., and Liu, Z. "Mesh Deformation on 3D Complex Configurations Using Multistep Radial Basis Functions Interpolation." *Chinese Journal of Aeronautics*, Vol. 31, No. 4, 2018, pp. 660–671. https://doi.org/10.1016/j.cja.2018.01.028.

[50] An, X., Deng, B., Feng, J., and Qu, Y. "Analysis of Nonlinear Aeroelastic Response of Curved Panels under Shock Impingements." *Journal of Fluids and Structures*, Vol. 107, 2021, p. 103404. https://doi.org/https://doi.org/10.1016/j.jfluidstructs.2021.103404.

[51] Abdukhakimov, F. A., and Vedeneev, V. V. "Effect of Yaw Angle on Flutter of Rectangular Plates at Low Supersonic Speeds." *AIAA Journal*, Vol. 60, No. 7, 2022, pp. 4256–4266. https://doi.org/10.2514/1.J061441.

[52] Bhatia, M., and Beran, P. "Transonic Panel Flutter Predictions Using a Linearized Stability Formulation." *AIAA Journal*, Vol. 55, No. 10, 2017, pp.

3499–3516. https://doi.org/10.2514/1.j055839.

[53] Davis, G., and Bendiksen, O. Transonic Panel Flutter. In *34th Structures, Structural Dynamics and Materials Conference*, American Institute of Aeronautics and Astronautics, 1993.

[54] Alder, M. "Development and Validation of a Fluid-Structure Solver for Transonic Panel Flutter." *AIAA Journal*, Vol. 53, No. 12, 2015, pp. 3509–3521. https://doi.org/10.2514/1.J054013.

[55] An, X., Xu, W., and Xu, M. "Analysis of Nonlinear Panel Flutter." *Hangkong Xuebao/Acta Aeronautica et Astronautica Sinica*, Vol. 36, No. 4, 2015, pp. 1119–1127. https://doi.org/10.7527/S1000-6893.2014.0221.